RSC Advances

ROYAL SOCIETY OF CHEMISTRY

www.rsc.org/advances

Highly Effective CO_2 Capture Using Super-fine PVDF Hollow Fiber Membranes with Sub-layer Large Cavities

Ali Ghodsi[a], Hossein Fashandi[a, *], Mohammad Zarrebini[a], Mohammad Mahdi Abolhasani[b], Mohsen Gorji[c]

[a.] Department of Textile Engineering, Isfahan University of Technology, Isfahan, 84156-83111, Iran

[b.] Department of Chemical Engineering, University of Kashan, Kashan, Iran

[c]. Polymer Engineering Group, Composite Science and Technology Research Center, MUT, Tehran, Iran

[*]. To whom correspondence should be addressed. E-mail: h.fashandi@cc.iut.ac.ir. Tel: +98-31-3391-1091. Fax: +98-31-33912444.

Abstract

This work reports a noticeable advancement in CO_2 capture using gas-liquid membrane contactors (GLMC) composed of super-fine poly(vinylidene fluoride) hollow fiber membranes (PVDF HFMs). This is accomplished by incorporating large cavities as sub-layer beneath the porous upper layer populated with macrovoids in a matrix of interconnected network of pores. Superimposing rheological images on ternary phase diagrams is considered as a promising and comprehensive tool for interpretation of the observed morphologies in HFs. Accordingly, the sub-layer cavities are evolved when the elastic modulus of HF outer layer (G_o') in contact with bore fluid is not high enough to dampen convective flows driven by the interfacial energy gradient. Implications of the impressive performance of drawing process on formation of the large cavities are discussed. Special attention is paid to the greater influence of increasing absorbent flow rate on enhancing CO_2 capture efficiency of HFs with large cavities.

Keywords: CO_2 absorption; Super-fine PVDF hollow fiber; large sub-layer cavity; ternary phase behavior; viscoelastic properties.

1. Introduction

Removal of carbon dioxide (CO_2) from gas streams has gained a growing interest due to sustained increase in sources emitting this gas. Abundance of CO_2 in the atmosphere has shown an ascending growth with an average rate of 1.4 ppm per year during the period of 1960 to 2005. Among various worldwide CO_2 emission sources, the industrial-related activities including burning of fossil fuels (coal, oil, natural gas) in power plants, gas flaring, cement, iron and steel production and chemical processes are considered to be the most primary source of CO_2 emission [1, 2].

The rise of greenhouse gases particularly CO_2 in the atmosphere is the basis of global awareness concerning possible climate changes and global warming. These have made CO_2 capture a worldwide issue [3].Therefore, efforts have been devoted to develop techniques for CO_2 absorption including adsorption of the gas using molecular sieves, solid adsorption, physical and chemical absorption, use of cryogenic processes, column absorption and finally membrane-based methods [3, 4]. Recent years have witnessed great deal of interest and progress on investigation of potential capabilities of hollow fiber membranes (HFMs) and development of robust and efficient HF-based gas-liquid membrane contactors (HF-GLMC) for CO_2 gas capture. Inside the HF-GLMC module, absorbent liquid and gas are allowed to flow counter-current to each other through lumen and shell sides of a microporous HF [5].The following advantages make HF-GLMC a superior choice for absorption of the main gaseous atmospheric contaminant, CO_2, and total mitigation of greenhouse gas emissions [4-8]:

- Large specific gas-liquid contacting area
- No further need for phase separation after CO_2 absorption due to streaming of gas and liquid through sequestered channels
- independent adjustment of gas and liquid flow rates
- no disruptive effect of gas and liquid flow rates on gas-liquid interfacial area
- Cost effective, easy to scale-up & -down and operationally flexible

In contrast to the above-mentioned advantages, the efficiency of HF-GLMCs as CO_2 absorber may be reduced by filling of pores with stagnant liquid, *i.e.* membrane wetting. Under this condition, high mass transfer resistance together with low diffusivity render the membrane useless. The wetting can be averted by using hollow fibers spun from highly hydrophobic polymers like poly(tetrafluoro ethylene) (PTFE) [9, 10]. Strictly speaking, the service time of HF-GLMC strongly depends on the extent of membrane hydrophobicity feature. PTFE

provides the highest degree of hydrophobicity and therefore the longest service time as established by Nishikawa *et al.* [9] who measured a stability about 6600 h for GLMC composed of PTFE HFMs. However, this polymer is too expensive with low processability mainly because of its insolubility in common solvents at low temperatures. This paved the way for other hydrophobic polymers with good processability including polypropylene (PP) [10 ,11], polyethersulfone (PES) [12], polysulfone (PSf) [13, 14] and polyetherimide (PEI) [15, 16] as well as recently non-polymeric HFs [17] to be used in construction of GLMCs.

Poly(vinylidene fluoride) (PVDF) has drawn extensive attention as another promising alternative to manufacture HF-GLMCs [4, 6, 7, 8, 18-30]. This polymer is advantageous due to its solubility in common solvents (ease of processability), high degree of hydrophobicity, thermal stability, high chemical resistance and mechanical strength, flexibility and the fair cost of production [31, 32]. A review of literature shows PVDF HFMs for CO_2 capture have been produced based on two different techniques, *i.e.* LIPS (liquid-induced phase separation) [4, 7, 8, 18-25, 27-30] and TIPS (thermally induced phase separation) [6, 8, 26]. Furthermore, it has been concluded that the former technique is more preferred. To our knowledge, up to now the following LIPS-related factors have been primarily addressed by scientific researches to elaborate PVDF HFM morphology and characteristics for construction of efficient GLMCs intended for CO_2 absorption:

- PVDF concentration and dope rheology [19]
- internal coagulant and inner skin of HF [18, 20]
- incorporation of additives in the spinning dope including: (1) Bulk modifier additives [4, 18-22, 24] and (2) surface modifier additives: a highly hydrophobic amphiphatic polymer with low surface tension known as SMM (surface modifying macromolecules) [4, 25, 27, 28] or nanoclay [29, 30].

- surface modification of HFMs thorough a post-treatment process [23]

In order to investigate the influence of membrane surface porosity on CO_2 absorption efficiency, Rajabzadeh *et al.* [6] prepared asymmetric PVDF HFs with different structures via the TIPS process. It was concluded that CO_2 absorption is affected by surface porosity just once the surface porosity contains very small values. Atchariyawut *et al.* [18] produced PVDF HFMs with a variety of morphologies using various additives including phosporous acid, glycerol and water. It was shown that CO_2 absorption performance and the ratio of membrane resistance to the total mass transfer resistance are inversely related. The former is in turn correlated to the MWCO (molecular weight cut-off) and the percentage of finger-like pores within the membrane structure. It was also emphasized that CO_2 absorption reduces with inner skin formation. In another study, Xu. et al. [20] demonstrated that inner skin-free PVDF HFMs are advantageous for CO_2 absorption and separation due to direct consequence of reduced resistance of membrane against gas transport.

The contribution of PVDF concentration and rheology on the CO_2 absorption of PVDF HFMs were examined by Ghasem *et al.* [8] and Ren *et al.* [19]. It was stated that, higher polymer concentration accounts for decreased mean pore size, effective surface porosity, void fraction and hence, CO_2 flux; conversely, liquid entry pressure of water (LEP_W), membrane density and thickness of PVDF HFMs outer surface are directly related to polymer concentration [8]. Furthermore, the positive impact of shear rate on elaborating PVDF HFM structure for more efficient CO_2 capture manifests itself at higher dope concentrations [19].

In recent years, surface modification of PVDF HFMs have attracted researchers' attention to develop HFMs with enhanced CO_2 capture performance [4, 23, 25, 27-30]. However, this method poses considerable challenges including surface modifier availability and synthesis along with high final cost of produced HFMs and the need for post treatment which all

restrict its versatility. Hence, the priority is given to production of PVDF HFMs from additive-free solutions through a single step process. In this respect, controlling of spinning solution parameters which directly affect HFM morphology, become prominent. Although some literature [19, 20] have focused on this area, but different aspects of solvent and PVDF properties contribution to design ultrafine HFMs for CO_2 absorption are still missing. Furthermore, production of PVDF HFMs from additive-free solutions is scarcely reported.

This work aims at production of superfine HFMs from additive-free solutions intended for more effective CO_2 absorption. This was implemented by incorporating macrovoids and sub-layer large cavities within the HF skeleton, noting the interplay of PVDF solution rheological properties and high stretching of spinning jet. The potential of the prepared HFs to capture CO_2 was investigated using GLMC modules by alteration of liquid absorbent flow rates.

2. Experimental

2.1. Materials

Two commercially available PVDF homopolymers with the same chemical structures -(-CH_2-CF_2-)$_n$- in two physical forms were supplied by Arkema® Inc.:

- PVDF1: Kynar® 761A Powder, M_w=495000 g/mole, MFI: 2.0-6.0 g/10 min (ASTM D1238, 230 ºC, 12.5 kg), Melting point: 165-172 ºC, Melt viscosity: 30-34 kPoise (ASTM D3835, @100 sec^{-1}, 230 ºC)
- PVDF2: Kynar® 740 Pellet, M_n=156000 g/mole, MFI: 6.0-25.0 g/10 min (ASTM D1238, 230 ºC, 12.5 kg), Melting point: 165-172 ºC, Melt viscosity: 15-23 kPoise (ASTM D3835, @100 sec^{-1}, 230 ºC)

Solvents dimethylformamide (DMF), N-methyl pyrrolidone (NMP) and 2-pyrrolidone (2P) were purchased from Sigma Aldrich, Inc. Distilled water was used as nonsolvent for polymer

solutions and as liquid for CO_2 absorption and permeation flux experiments. All chemicals were used as received with no further purification.

2.2. Phase behavior of ternary systems

Thermodynamic Phase behavior of ternary nonsolvent (1)/solvent (2)/polymer (3) systems was investigated based on the classical Flory-Huggins (FH) model expanded by Tompa [33]. According to this model, the Gibbs free energy of mixing (ΔG_M) can be formulated as Eq. 1

$$\frac{\Delta G_M}{RT} = n_1 ln\varphi_1 + n_2 ln\varphi_2 + n_3 ln\varphi_3 + n_1\varphi_2 g_{12}(u_2) + n_2\varphi_3\chi_{23} + n_1\varphi_3\chi_{13} \quad (1)$$

In Eq. 1, n_i and φ_i stand for the number of moles and the volume fraction of component *i,* respectively; *R* and *T* are the universal gas constant (8.314 *J/mol.K*) and the absolute temperature (*K*), respectively. χ_{23} represents the interaction parameter of a binary mixture of solvent(2) and polymer(3) which is considered to be concentration-independent in this work. Further, χ_{13} points to the nonsolvent(1)/polymer(3) interaction parameter, often assumed as a constant. Finally, $g_{12}(u_2)$ is a generalized nonsolvent(1)/solvent(2) interaction parameter depending on the volume fraction $u_2 = \varphi_2/(\varphi_1 + \varphi_2)$ of a pseudo binary mixture [34, 35].

As obvious, estimation of ΔG_M as well as its derivatives for a given ternary system at temperature of interest needs the above-mentioned interaction parameters, *i.e.* χ_{23}, χ_{13} and $g_{12}(u_2)$, to be known. In the present contribution, g_{12} for water/DMF, water/NMP and water/2P pairs were calculated based on either Eq. 2 or Eq. 3 whose associated coefficients for temperature of 20 °C were collected from literature [35-38].

$$g_{12}(u_2) = \alpha + \frac{\beta}{1 - \gamma u_2} \quad (2)$$

$$g_{12}(u_2) = \alpha + \beta u_2 + \gamma u_2^2 + \varepsilon u_2^3 + \zeta u_2^4 \quad (3)$$

Eq. 4 was considered to obtain $\chi_{DMF/PVDF}$ and $\chi_{NMP/PVDF}$ while $\chi_{2P/PVDF}$ was adjusted to closely fit the calculated binodal curve with the experimentally measured cloud points.

$$\chi_{23} = 0.35 + \frac{v_2}{RT}(\delta_2 - \delta_3)^2 \quad (4)$$

In Eq. 4, v_2 stands for the solvent molar volume and δ_i $(i = 2, 3)$ represents the solubility parameter of component *i*. The literature values of $\delta_{PVDF} = 23.2\ (MPa)^{0.5}$, $\delta_{DMF} = 24.8\ (MPa)^{0.5}$ and $\delta_{NMP} = 22.9\ (MPa)^{0.5}$ were used [39]. Equilibrium water uptake of PVDF film was regarded as a well-accepted and convenient technique for estimation of $\chi_{water/PVDF}$. The procedure was detailed in our previous works [37, 40]. Construction of thermodynamic phase diagrams consisting of binodal and spinodal boundaries along with associated tie-lines was achieved using the mathematical/numerical algorithm successfully employed in Ref. [40]. Summary of the interaction parameters used in this work are listed in Table 1.

Table 1. Interaction parameters used to construct ternary phase diagrams of different ternary systems at 25 °C

Ternary system	$g_{12}(u_2)$	χ_{13}	χ_{23}
water/DMF/PVDF	$g_{12}(u_2) = 0.50 + 0.04u_2 + 0.80u_2^2 - 1.20u_2^3 + 0.8u_2^4$ [35]	2.6± 0.2	0.4
water/NMP/PVDF	$g_{12}(u_2) = (\alpha = 0.316) + \frac{\beta = 0.468}{1-(\gamma = 0.499)u_2}$ [36, 37]	2.6± 0.2	0.35
water/2P/PVDF	$g_{12}(u_2) = (\alpha = 0.32) + \frac{\beta = 0.47}{1-(\gamma = 0.5)u_2}$ [38]	2.6± 0.2	0.3

Calculated binodal curves were further checked by experimentally measured cloud points. To obtain cloud points, water was added dropwise (while stirring) to PVDF solutions of various concentrations ranging from 1 to 20 wt.%, until the initial homogeneous solution turned

turbid. Throughout the experiment, the temperature of solution was kept constant at 25 ^{o}C. The turbidity concentrations were recorded as cloud points.

The crystallization-induced gelation boundary at 25 ^{o}C was also experimentally determined using a simple and well-known method [41]. To this end, the PVDF solution with a given concentration in the range of 1-20 wt.% was agitated with a specific amount of water. The mixture temperature was raised to ca. 60 ^{o}C at which complete dissolution occurred. This was followed by aging of the homogeneous clear solution in a chamber with constant temperature (25 ^{o}C) for a week. The addition of water was continued until the solution turned into a gel. The gelation point was simply qualitatively determined by visual inspection of cessation of the liquid flow in a tilting glass tube. The gelled concentrations were recorded as crystallization-induced gelation points which are connected together by the gelation boundary.

2.3. Characterization of spinning solutions and gels

2.3.1. Evaluation the viscoelastic properties

Oscillatory rheometer, MCR 301 (Anton Paar Co., Germany) equipped with two parallel plates, was employed to evaluate viscoelastic characteristics of spinning solutions and gels. All experiments were performed at constant temperature of 25 ºC. The storage (G') and loss (G'') moduli were measured at a fixed amplitude of 5% and a swept frequency of 0.01 to 100 Hz. Prior to the frequency sweep tests, an amplitude scanning was conducted to ensure the linearity of dynamic viscoelasticity.

2.3.2. Zero-shear viscosity of spinning solutions

The shear viscosity of spinning solutions as a function of shear rate, was determined using Rotovisco RV12 viscometer (HAAKE, Germany) at controlled temperature of 25 ºC ($\pm$2 ºC). Zero shear viscosities (η_0) of spinning solutions were extracted by extrapolating to zero shear rates.

2.4. Hollow fiber spinning

The PVDF powder (PVDF1) and granules (PVDF2) were dried in a vacuum oven for 24 h at 60 ºC to remove the moisture content. Homogeneous spinning solution was prepared by mixing given amounts of PVDF and solvent under gentle stirring at 70 ºC for 24 h. The specifications of the spinning solutions are given in Table 2. Before spinning, the clear resultant solution was degassed at room temperature for 48 h. Fabrication of HFs was carried out by extruding of the polymer solution through an annular gap of a spinneret with two concentric orifices into the external coagulation bath using a precision gear pump (0.3 ml/Rev.). Bore fluid was injected into the interior orifice of spinneret using a highly accurate syringe pump. The spinning parameters in detail are listed in Table 3.

In order to achieve complete solvent exchange and avoid shrinkage during drying period, the fabricated HFs were immersed sequentially into ethanol/water (50:50), pure ethanol and finally ethanol/n-hexane (50:50). The HFs were then dried at room temperature before some characterization tests.

Table 2. Specifications of spinning dopes

HF ID code	Spinning dope [a]	PVDF type	Solvent	Polymer concentration (wt.%)	Polymer concentration (φ_p)[b]	Zero-shear viscosity (η_0) (mPa.s)
HF1	L	1	DMF	10	0.055	400
HF2	J		NMP		0.060	1300
HF3	H		2P		0.065	2000
HF4	F	2	DMF	20	0.117	100
HF5	D		NMP		0.126	506
HF6	A		2P		0.136	960

[a.] The spinning dopes have been localized on ternary phase diagram illustrated in Fig. 16.
φ_p refers to polymer volume fraction.

Table 3. HF Spinning parameters

Spinning parameter	Value
Spinneret inner diameter (*i.d.*) (mm)	0.7
Spinneret outer diameter (*o.d.*) (mm)	1.3
Bore fluid	Distilled water
External coagulation bath	Tap water
Dope extrusion rate (ml/min)	2.4
Bore fluid flow rate (ml/min)	0.65
Air-gap distance (cm)	18
Spinning dope temperature (ºC)	25
Bore fluid temperature (ºC)	25
External coagulation bath temperature (ºC)	25
Take-up speed (m/min)	20

2.5. Characterization of HFMs

2.5.1. Scanning electron microscopy (SEM)

The inner and outer surfaces along with cross-sections of prepared HFs were examined using scanning electron microscope (SEM) (TESCAN series VEGA 2007 from Czech) performed at 30 kV acceleration voltage. Prior to imaging, samples were sputter-coated with a 10 nm layer of gold. To monitor the HF cross-section, it was cryogenically fractured in liquid nitrogen and then examined by SEM.

2.5.2. Measurement of overall porosity

HFs were characterized for their overall porosities (ε) based on gravimetric method. ε is defined as the ratio of the pore volume to the total volume of the fiber and can be estimated using Eq. 5.

$$\varepsilon(\%) = \frac{(w_w - w_D)/\rho_w}{[\frac{w_w - w_D}{\rho_w} + \frac{w_D}{\rho_p}]} \times 100 \quad (5)$$

where w_w and w_D indicate to weights of wet and dry hollow fibers, respectively. ρ_w and ρ_p stand for densities of water and polymer, respectively. To obtain w_w, fibers were weighed after immersing in oil for 24 h and removing the remaining liquid on the outer surfaces of fibers. Air was blown to the lumen side of HFs to eliminate the extra water. Reproducibility

of the measurements was assured by taking the average over 5 measurements for each sample.

2.5.3. Gas permeation test

The mean pore size as well as effective surface porosity of the prepared HFs was estimated based on gas permeation test. Polyurethane resin was used to block one end of ten HFs each with the effective length of about 11 cm. The ten HFs were potted into a 21 cm stainless steel tubular module. A pressure regulator before the module was used to feed N_2 in the range of 0.25-2 bar to the shell side of the module. Lumen permeation of HFs was determined at 25 ºC using a highly accurate rotameter flow meter. Equations concerning calculation of mean pore size and effective surface porosity of HFMs have been detailed by Li [42] and used by many researchers [4, 8, 13, 21, 22, 24, 25, 26, 28, 29]. These equations are based on straight and cylindrical pores. Furthermore, gas permeation is assumed to be under the Poiseuille and Knudsen flow regimes in parallel connection. Hence, the overall N_2 permeation can be estimated based on Eq. 6.

$$J_A = \frac{2r_P\varepsilon}{3RTL_P}\left(\frac{8RT}{\pi M}\right)^{0.5} + \frac{r_P^2\varepsilon}{8\mu RTL_P}\bar{P} \quad (6)$$

where J_A indicates to N_2 permeance (mol/m^2.Pa.s); r_P and L_P stand for pore radius (m) and effective pore length (m), respectively. ε is surface porosity; T is gas absolute temperature (K) and R is gas constant 8.314 (J/mol.K). μ and M are gas viscosity (Pa.s) at temperature T and gas molecular (g/mol), respectively. Eq. 6 can be reduced as Eq. 7.

$$J_A = K_0 + P_0\bar{P} \quad (7)$$

In Eq. 3, $\bar{P}$ is mean pressure (Pa). Plotting of J_A versus $\bar{P}$ provides the slope (P_0) and intercept (K_0) of the line. These yield to calculation of mean pore size (r_P) and effective surface porosity (ε/L_P) of HFMs by use of Eqs. 8 and 9, respectively. It should be noted gas permeability was calculated in terms of the outer diameter of HFs.

$$r_P = 5.33\left(\frac{P_0}{K_0}\right)\left(\frac{8RT}{\pi M}\right)^{0.5}\ \mu \tag{8}$$

$$\frac{\varepsilon}{L_P} = \frac{8\mu RTP_0}{r_P^2} \tag{9}$$

2.5.4. Pure water permeability (PWP) evaluation

The schematic diagram of apparatus used to measure PWP is shown in Fig. 1. Ten HFs with effective length of 18 cm were potted into a transparent tubular module using polyurethane resin. Distilled water was fed into the shell side of the HFs at pressure of 1.2 bar using a diaphragm pump and water permeation through the lumen sides of HFs over a given length of time was measured. The permeability of HFMs for pure water (J_w) ($L.m^2.h^{-1}.bar^{-1}$) is defined by Eq. 10.

$$J_w = \frac{Q}{\Delta P.A} \tag{10}$$

where Q stands for volumetric permeation rate of pure water ($L.h^{-1}$); ΔP and A are the transmembrane pressure (*bar*) and the effective area of the HFMs (m^2).

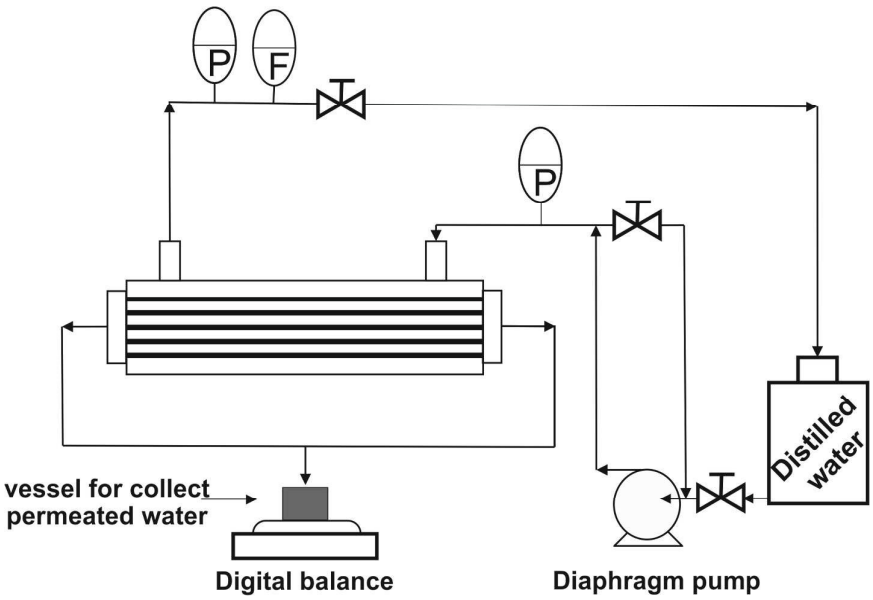

Figure 1. Schematic flow diagram of experimental setup for measuring pure water permeability (J_w).

2.5.5. Measurement of critical water entry pressure (CEP_w)

CEP_w was measured using the same module that used in preceding section. Distilled water was pumped into the lumen side of HFs. The water pressure was increased stepwise at 0.5 bar interval. CEP_w was recorded as the pressure at which the first droplet of water appears on the outer surface of HFs. To check appearance of water droplets, the module was kept at constant pressure for 30 min. This technique has been

2.5.6. Evaluation of mechanical properties and stability

The mechanical properties of produced HFs were evaluated using Zwick tensile testing machine (model: 1446-60). The initial distance between clamps and stretching rate were adjusted at 2.5 cm and 50 mm/min, respectively. Experimental errors were minimized by repeating the measurements six times for each sample before the mean value was calculated.

The mechanical stability of HFs was assessed on the same module that was used for gas permeation test. This was implemented according to the results of collapsing pressure test during which the upstream gas (N_2) pressure in the shell side of module was increased at 0.5 bar interval. An unexpected increment or decrease in the permeate flow was regarded as collapsing pressure.

2.5.7. FTIR (Fourier transfer infrared) spectroscopy

Crystal polymorphism of PVDF HFMs was examined by recording attenuated total reflectance (ATR) spectrum using BOMEM FTIR MB-series, MB-100 (Hartmann & Braun, Canada). The HF samples were put directly on the surface of a flat crystal (ZnSe, a 45° ATR prism). The spectrum was measured at a wavenumber resolution of 4 cm^{-1} for spectral range of 2000 to 700 cm^{-1}. For quantitative analysis, all FTIR spectra were normalized using the peak at 877 cm^{-1} as reference band [43].

2.5.8. Measurement of water contact angle

Dynamic contact angle of water on HFMs outer surface was measured using a tensiometer (DCAT 11, Dataphysics, Germany) from the wetting force based on the Wilhelmy technique. A piece of HF approximately 5 cm long was hung from the rod of a highly accurate electro-balance, and was then immersed into DI water. The weight difference was continuously recorded. The interfacial moving rate and immersion depth were selected to be 0.2 mm/min and 5 mm. In order to ensure the reproducibility within the statistical deviation, for each sample the experiment was repeated three times.

2.5.9. CO_2 absorption experiment

The schematic of gas-liquid membrane contactor used for evaluation CO_2 absorption of prepared HFMs is illustrated in Fig. 2. A total of ten HFs were packed in the module same as that used in sections 2.5.4. and 2.5.5. The module specifications are detailed in Table 4. Pure CO_2 and distilled water were used as feed gas and liquid absorbent on the lumen and shell sides of HFs, respectively. In order to avoid bubble formation in the liquid, the gas side and liquid side pressures were adjusted to be 1 bar and 1.2 bar, respectively. The gas flow rate was kept constant at 11 L/h throughout the experiment while the liquid flow rate was varied in the range of and 3-12 L/h. The gas and the liquid were allowed to come into contact with each other in a counter current mode. Steady state conditions were achieved by conducting experiments for 30 min prior to sampling. The CO_2 concentration in the absorbent liquid was determined using chemical titration method. NaOH (0.05 M) was considered as titrant at the presence of phenolphetalein as indicator. The CO_2 concentration in liquid outlet ($C_{l,0}$) (mol/m^3) and CO_2 flux (J_{CO_2}) are correlated through Eq. 11.

$$J_{CO_2} = \frac{Q_{l,}.C_{l,0}}{A_0} \tag{11}$$

where Q_l stands for liquid flow rate (m^3/s) and A_0 indicates to the outer surface of HFs (m^2). To ensure the reproducibility of obtained data, CO_2 absorption test was repeated five times for each HF. The reported results have been averaged over 5 measurements.

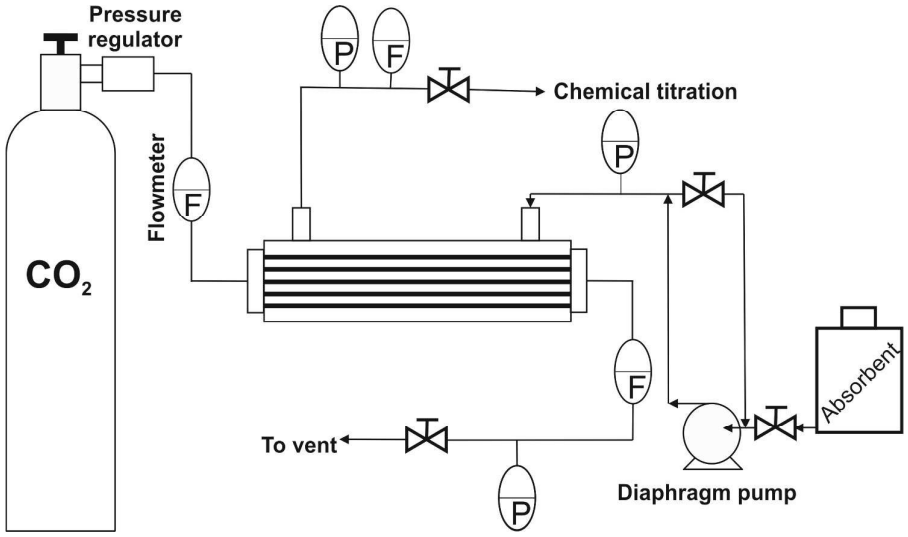

Figure 2. Schematic flow diagram of experimental setup for CO_2 absorption.

Table 4. Characteristics of gas-liquid membrane contactor module

Parameter	Value
Module inner diameter (i.d.) (mm)	14
Module length (mm)	210
HF outer diameter (i.d.) (mm) (listed in Table 5)	0.314-0.421
Effective fiber length (mm)	180
Number of fibers	10
Packing density (%)	0.50-0.90

The membrane mass transfer resistance was quantitatively investigated according to Wilson plot technique [44, 4, 7]. To this end, the inverse of overall mass transfer resistance (K_0), *i.e.* liquid and membrane mass transfer resistance, was plotted versus $V_l^{-\alpha}$ where V_l and α are the absorbent velocity and an empirical constant, respectively. The latter is chosen as the one which provides the best straight line through the experimental data points. The graph is known as Wilson plot whose intercept gives the membrane mass transfer resistance. Since pure CO_2 is used in the lumen side of HFs, the gas side mass transfer resistance can be disregarded [4, 7]. K_0 can be expressed by Eq. 12 [4, 7, 45].

$$K_0 = -\frac{Q_l}{A_O} ln\left(1 - \frac{C_{l,0}}{HC_g}\right) \quad (12)$$

In Eq. 12, Q_l and A_O refer to liquid flow rate (m^3/s) and gas-liquid contact area, *i.e.* outer surface of HFs (m^2), respectively; C_g and $C_{l,0}$ are gas side and liquid outlet concentration (mol/m^3); H stands for Henry's law constant. For CO_2/water system, H is regarded to be 0.85.

3. Results and Discussion

3.1. Structural and performance characteristics of prepared HFs

The SEM images of HFs spun from 10 wt.% PVDF1 solutions in three different solvents, *i.e.* DMF (HF1), NMP (HF2) and 2P (HF3), are shown in Figs. 3 to 5. It can be clearly seen from Figs. 3a, 4a and 5a, the walls of HFs can be divided into two adjacent layers, irrespective of solvent type. The sub-layer encompasses large cavities, and the top layer is composed of an interconnected network of pores (magnified in Figs. 3d, 4d and 5d) occupied by macrovoids. This type of morphology is schematically depicted in Fig. 6. In general, Figs. 3-5 point to existence of the following common features in the HF1, HF2 and HF3:

- Super-fine HFs with thin wall of approximately 70 μm
- Structurally composed of large cavities and interconnected network of pores making up the sub-layer and top layer, respectively
- Dense and nonporous outer surfaces as shown in Figs. 3e, 4e, 5e

Despite these common features, the HFs exhibit significant structural differences as follow:

- As vividly shown by Figs. 3a, 3c, 4a & 5a, macrovoid density in HF top layer changes with solvent used. Specifically, the HF spun from DMF-based solution, has no macrovoids within its top layer, whereas considerable areas of HF2 and HF3 top layers in the vicinity of the outer surfaces are filled with macrovoids.

- In contrast to HF2 and HF3, the top layer of HF1 has been covered by a dense and nonporous skin as indicated by red arrow in Figs. 3c.
- Comparison of Figs. 3d, 4d & 5d, reveals the smaller size of interconnected pores of HF3 spun using 2P-based solution.
- The sub-layer cavities have been separated from the central bore through an inner boundary whose thickness varies with solvent type. Figs. 3a, b show thickest boundary is formed when DMF is used. The use of NMP and 2P as illustrated in Figs. 4a, b and 5a, b, results in formation of thinner and corrugated boundaries.

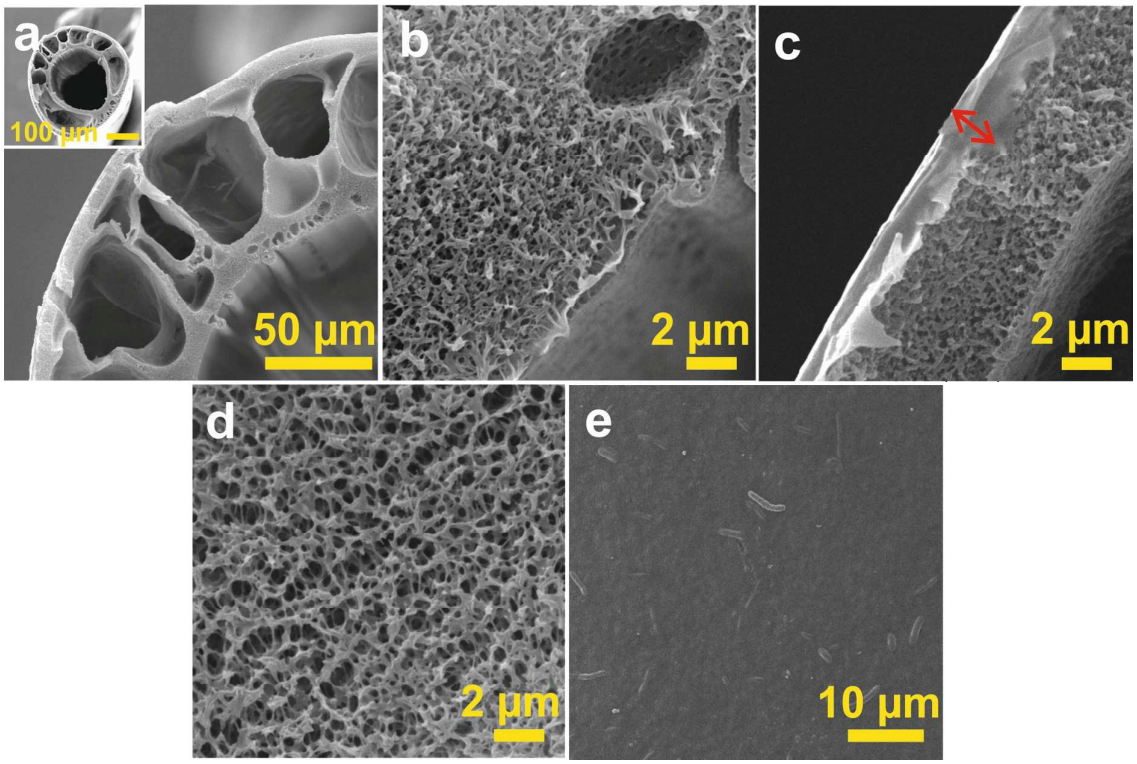

Figure 3. SEM images of HF1 (spun from PVDF1/DMF solution (10 wt.%)): (a) HF1 cross-section, (b) HF1 inner edge, (c) HF1 outer edge, (d) magnified porous zones, (e) HF1 outer surface.

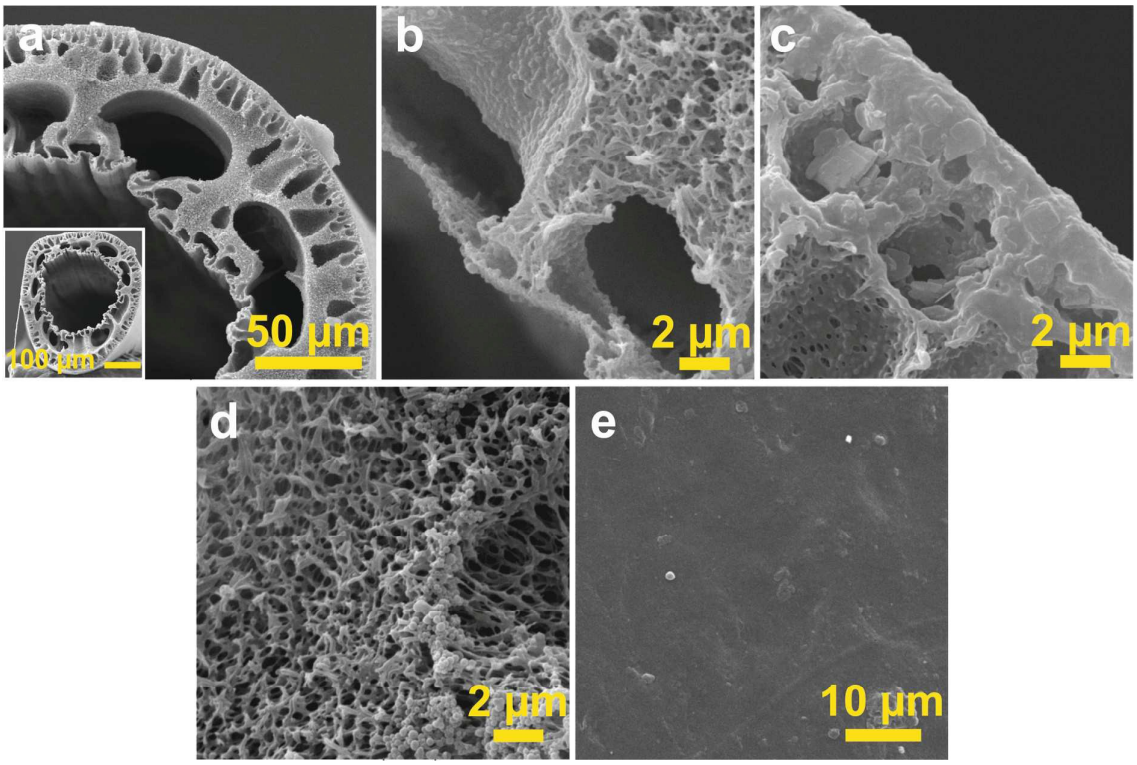

Figure 4. SEM images of HF2 (spun from PVDF1/NMP solution (10 wt.%)): (a) HF2 cross-section, (b) HF2 inner edge, (c) HF2 outer edge, (d) magnified porous zones, (e) HF2 outer surface.

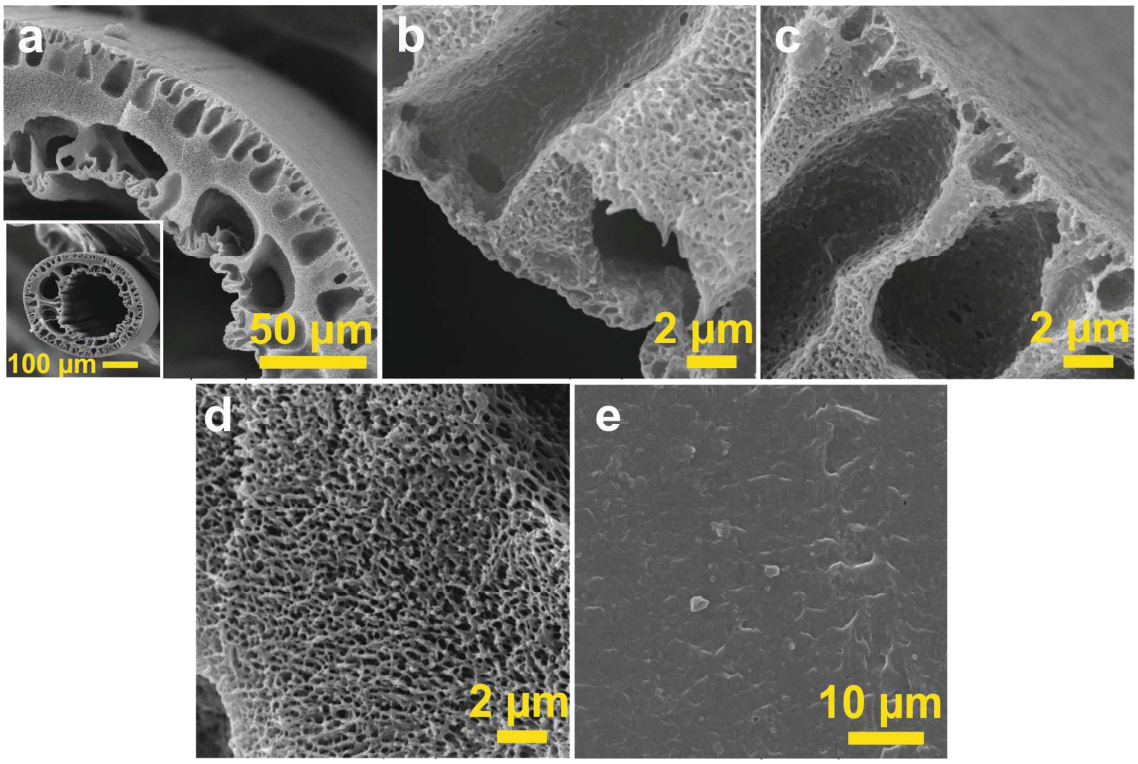

Figure 5. SEM images of HF3 (spun from PVDF1/2P solution (10 wt.%)): (a) HF3 cross-section, (b) HF3 inner edge, (c) HF3 outer edge, (d) magnified porous zones, (e) HF3 outer surface.

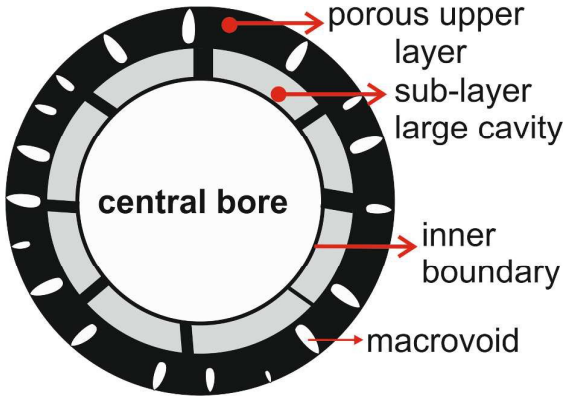

Figure 6. Schematic representation of structure of HF with a sub-layer large cavities and top layer occupied by macrovoids.

The morphology of HF4, HF5 and HF6 spun from PVDF2-based solutions is investigated in Figs. 7-9. As evident, irrespective of solvent type, using PVDF2 instead of PVDF1 together with changes in volume fraction of PVDF in the spinning dope (Table 2), results in the elimination of sub-layer large cavities. Strictly speaking, it can be said the sub-layer large cavities are replaced with smaller ones. These differences are confirmed when SEM images included in Figs. 7-9 are compared with corresponding ones in Figs. 3-5. Moreover, the interconnected networks of pores displayed in Figs. 3d, 4d & 5d are replaced by independent cellular pores shown in Figs. 7d, 8d and 9d. Apart from these differences, corrugated inner surfaces (Figs. 7a, 8a & 9a) and nonporous morphology for outer surfaces (Figs. 7e, 8e, 9e) are also observed for all HFs spun from solutions of PVDF2.

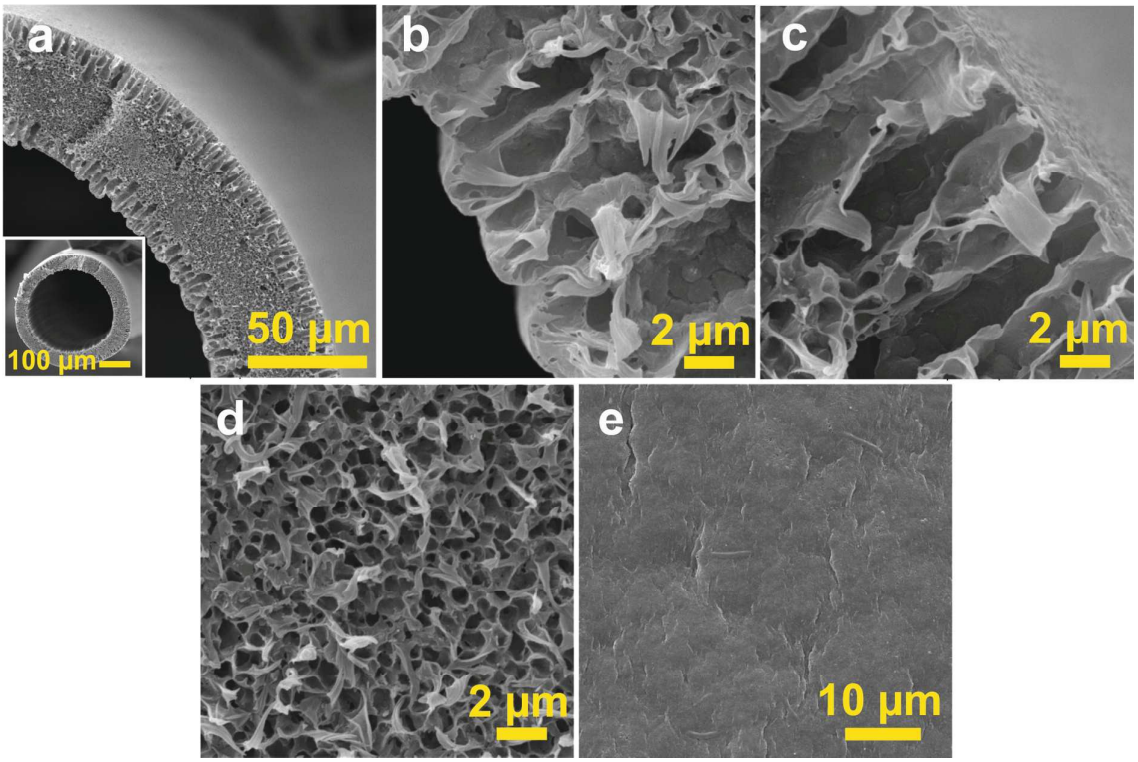

Figure 7. SEM images of HF4 (spun from PVDF2/DMF solution (20 wt.%)): (a) HF4 cross-section, (b) HF4 inner edge, (c) HF4 outer edge, (d) magnified porous zones, (e) HF4 outer surface.

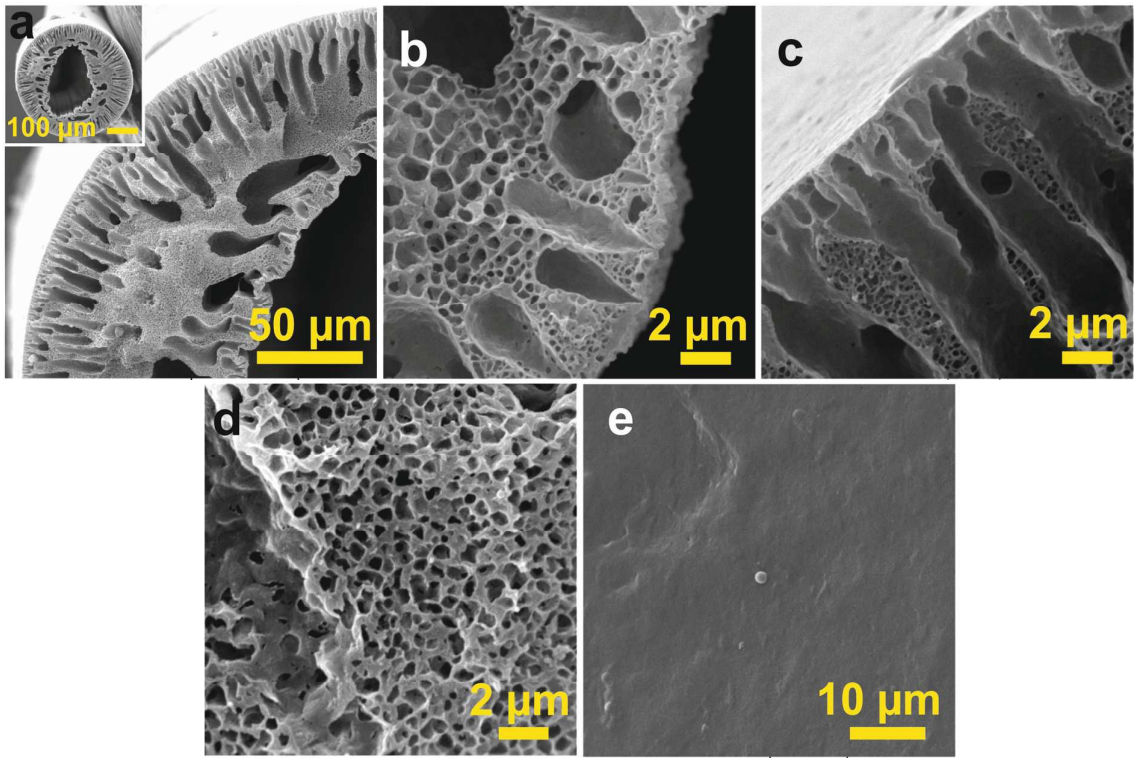

Figure 8. SEM images captured from HF5 (spun from PVDF2/NMP solution (20 wt.%)): (a) HF5 cross-section, (b) HF5 inner edge, (c) HF5 outer edge, (d) magnified porous zones, (e) HF5 outer surface.

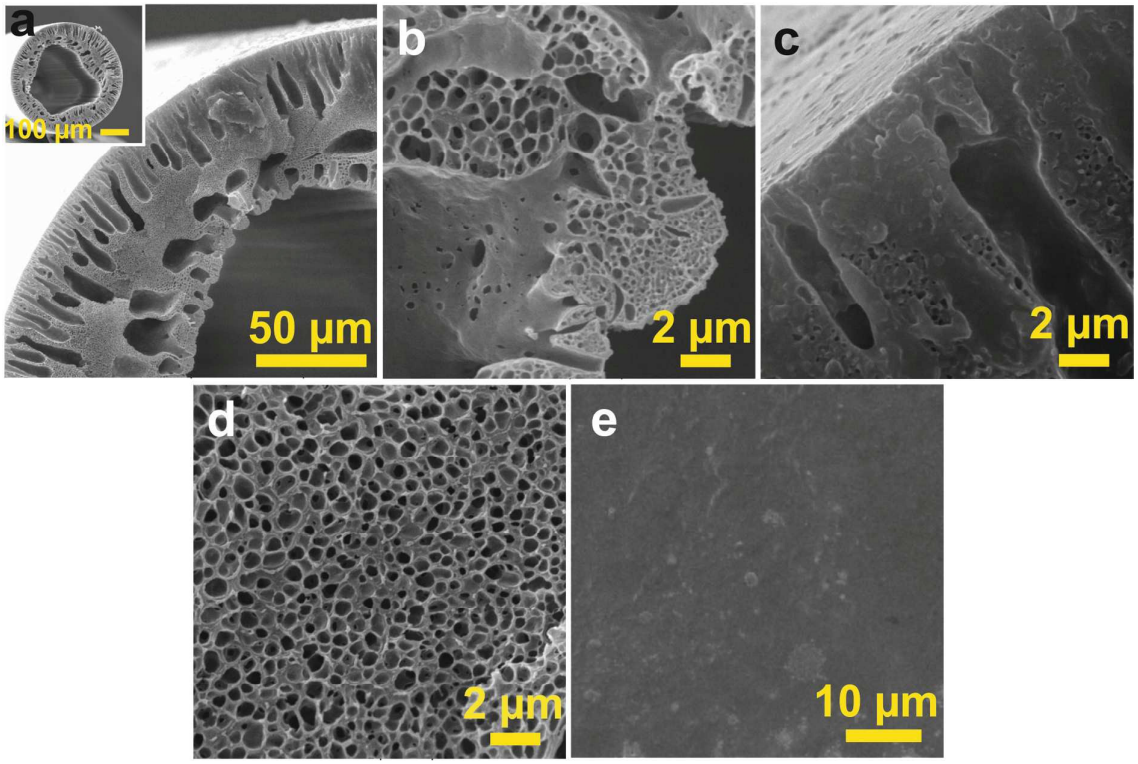

Figure 9. SEM images captured from HF6 (spun from PVDF2/2P solution (20 wt.%)): (a) HF6 cross-section, (b) HF6 inner edge, (c) HF6 outer edge, (d) magnified porous zones, (e) HF6 outer surface.

In order to further establish the effect of solvent and polymer type on morphology evolution and performance of spun HFs, structural and physical characteristics of the HFs together with their performance features are compared in Table 5. Table 5 vividly confirms the fineness superiority of spun HFs over the HFs reported in the previous researches listed in Table 7. This claim is further supported by the fact that, considering experimental measurement errors the thickness of all HF walls with the exception of HF5 lies in the range of 54-86 µm. It should be emphasized for HFs with bore of irregular shape like HF5, the inner diameter and wall thickness were averaged over at least five measurements from different parts of bore cross-section.

In Fig. 10 the variation of HFs mechanical properties and collapsing pressure has been plotted against corresponding values of overall porosity. It can be seen that there is an

acceptable correlation between the formers with the latter in form of an inverse linear relationship. It may be concluded that structures such as pores, voids and cavities which form the overall porosity of the HF skeleton, are in fact points of stress concentration that from mechanical point of view serve to weaken the HFs.

The fineness superiority of spun HFs, may raise the concerns about the suitability of spun HFs for CO_2 capture purposes. On the other hand, although HFMs with larger pores and smaller diameters are favored from point of enhanced gas permeation, but they are suspected to have less mechanical and wetting resistant corresponding to short service life. However, the measured values for mechanical properties, PWP, CEP_w and water contact angle of the spun HFs (Table 5) are comparable with those reported in literature (see Refs. cited in Table 7). Therefore, all the claims made in respect of the prepared HFs can be fully justified.

The N_2 permeation curves against mean pressure measured for prepared HFs, have been shown in Fig. 11. Additionally, the corresponding quantities of r_p and ε/L_p have been listed in Table 5. Regardless of HF type, all N_2 permeance curves included in Fig. 11 show a growing trend with increase in mean pressure. This behavior points to prevailing of both Poiseuille and Knudsen flows principles during N_2 permeation through the HFs. However, the higher slops of graphs associated to HF1 and HF2 denote to dominant contribution of Poiseuille flow. This happens when large cavities are present within HF structure which agrees well with SEM images illustrated in Figs. 3, 4 and 5. In contrast, HF4-, HF5- and HF6-related lines exhibit a gradual rising with increasing pressure highlighting the more prominent contribution of Knudsen flows through the membrane pores. The controlling effect of Knudsen flow becomes more intensified when no macrovoids are present within HF morphology as observed for HF4 (see Fig. 7). Strictly speaking, the noticeable reduction in N_2 permeance (shown in Fig. 11) together with small values of r_p and ε/L_p (reported in Table

5) for HF4, vividly confirm the pivotal importance of macrovoids and cavities in relation to enhanced gas permeation.

Totally, as evident from Table 5, comparing both structural features (mechanical properties, overall porosity, collapsing pressure, CEP_w and PWP) and N_2 permeation-related properties (r_p and ε/L_p) of different HFs, one can confirm the great contribution of both (1) solvent and (2) PVDF type as well as concentration. For example, the observed morphological and performance differences between HF4 and HF1, both of which have been spun from DMF-based solutions, point to the influence of PVDF type as well as concentration. Furthermore, comparing characteristics of HFs produced from (PVDF1) or (PVDF2), *i.e.* (HF1, HF2 and HF3) or (HF4, HF5 and HF6), respectively, the contribution of solvent to morphology evolution of HFs becomes clear. In summary it can be concluded that solvent and PVDF type as well as concentration affect the HF performance and properties through altering ternary phase behavior and rheological properties of initial spinning solutions and phase separated domains. These parameters have been fully discussed in section 3.2.

Table 5. Structural, physical and performance characteristics of the spun HFs

	HF1	HF2	HF3	HF4	HF5	HF6
Inner diameter (μm)	193	214	183	311	188	235
Outer diameter (μm)	329	356	314	418	421	407
Wall thickness (μm)	68	71	66	54	116	86
Max. stress (MPa)	3.4	2.4	3.0	4.9	2.5	3.9
Strain at break (%)	183.9	138.3	148.3	271.9	104.6	190.5
Young's modulus (Tensile modulus) (MPa)	85.8	86.6	103.5	163.8	77.4	108.7
Overall porosity (%) (STD*)	74.4 (0.03)	75.9 (0.01)	76.0 (0.02)	60.0 (0.04)	85.7 (0.06)	75.4 (0.01)
Average pore size (r_P) (nm)	104	112	90	39	67	67
Effective surface porosity (ε/L_P) (m^{-1})	225	279	175	160	233	233
Water contact angle (outer surface) (°)	86±1.5	88±1.4	85±1.5	88±1.2	89±1.5	85±1.3
Collapsing pressure (bar)	4.5±0.3	4±0.2	4±0.2	6±0.2	4±0.3	5±0.4
CEP_w (bar)	4±0.3	4±0.5	3.5±0.3	6±0.5	5±0.3	5±0.2
PWP (L/m^2.bar.h)	26.9	5.9	5.9	0.0	2.7	1.8

*. STD indicates to standard deviation

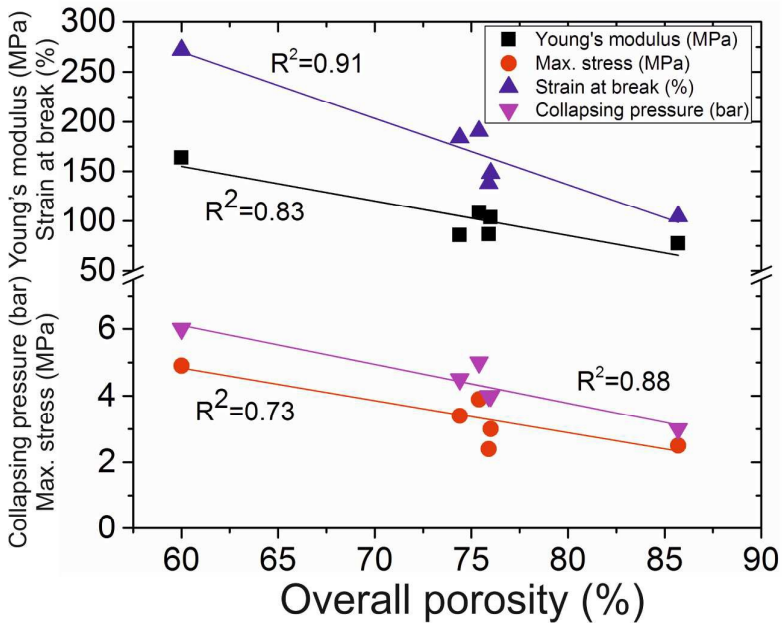

Figure 10. Variation of HFs mechanical properties as well as collapsing pressure versus HF overall prosity.

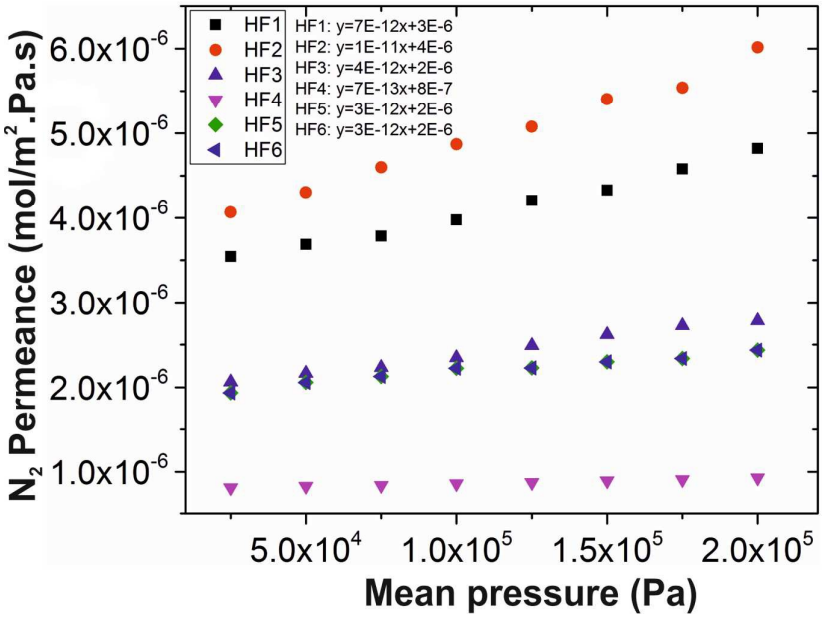

Figure 11. N_2 permeance as a function of mean pressure measured for spun HFs.

Included in Fig. 12 are CO_2 flux of produced HFs with different structures as a function of flow rate of distilled water used as absorbent. Obviously, for all HFs the CO_2 absorption efficiency increases with absorbent flow rate. Similar behavior was also reported in literature [4, 6, 7, 18, 21, 28]. This confirms the dominant effect of liquid phase resistance on the mass transfer process using GLMC. Strictly speaking, during physical absorption based on GLMC technique, a thin film around the gas-liquid interface creates the area for mass transfer. At higher velocities of liquid absorbent the thickness of the liquid boundary layer diminishes. This results in increase in the liquid mass transfer coefficient, and thus more efficient CO_2 absorption. This event has been fully argued elsewhere, *e.g.* Ref. [21].

As evident from Fig. 12, the maximum CO_2 flux was achieved by HF2. Contrarily, the CO_2 absorption by HF4 was extremely low which was considered as zero and not plotted in Fig. 12. Other spun HFs can be considered intermediate to these extremes, *i.e.* HF2 and HF4. Additionally, HF5 and HF6 achieve approximately the same performance for CO_2 absorption within experimental errors. This similarity in CO_2 capture agrees well with SEM images

(compare Figs. 8 and 9) as well as results of gas permeation tests (compare values of r_p and ε/L_p (Table 5) measured for HF5 and HF6 using graphs in Fig. 11). Totally, it can be stated that CO_2 absorption of spun HFs in ascending order is as follows:

- Ascending order of CO_2 absorption: HF4<HF6≈HF5<HF3<HF1<HF2

This order is fully in accordance with the ascending order of r_p and roughly concurs with the ascending order of ε/L_p (Table 5) as follows:

- Ascending order of r_p: HF4<HF5=HF6<HF3<HF1<HF2
- Ascending order of ε/L_p : HF4<HF3<HF1<HF5=HF6<HF2

The above established correlation states that differences observed between CO_2 absorption capabilities of prepared HFs can be best explained by structural differences as confirmed by N_2 permeation-related data, *i.e.* r_p and ε/L_p .

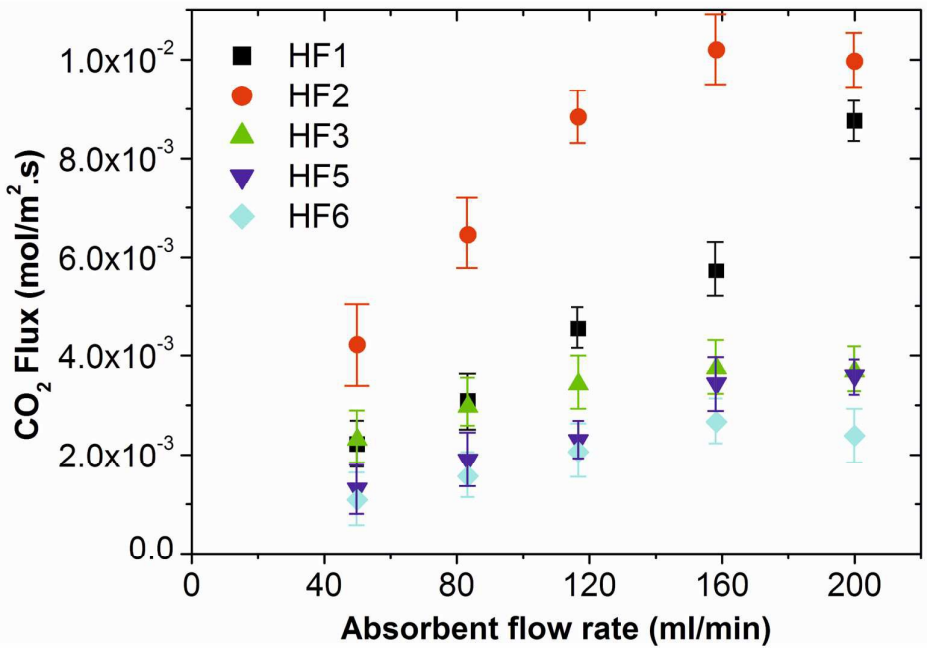

Figure 12. Effect of absorbent flow rate on CO_2 flux in the gas-liquid membrane contactor.

The Wilson plot for HFs produced in the present contribution has been displayed in Fig. 13. Value of α=0.93 for all HFs was found to linearly fit the data of Wilson plots ($1/K_0$ vs. $V_l^{-\alpha}$ described in section 2.5.9) with high accuracy. An analogous relationship, *i.e.* $1/K_0$ vs. $V_l^{-0.93}$, was also regarded by other researchers [13, 21, 28, 47]. As explained in section 2.5.9, the membrane mass transfer resistance for the prepared HFs was calculated from the intercept of Wilson plot with y-axis as listed in Table 6. According to this table, HF1 and HF3 provide the least and the most resistance against mass transfer, respectively. Overall, the membrane mass transfer resistance increases based on the order of HF1<HF2<HF5<HF6<HF3<HF4. This approximately but not exactly corresponds to the decreasing order of CO_2 absorption by prepared HFs.

Table 6. Calculated membrane mass transfer resistance of the prepared HFMs

HF ID code	HF1	HF2	HF3	HF5	HF6
Membrane mass transfer resistance (s/m)	1428	2814	15527	7604	13237

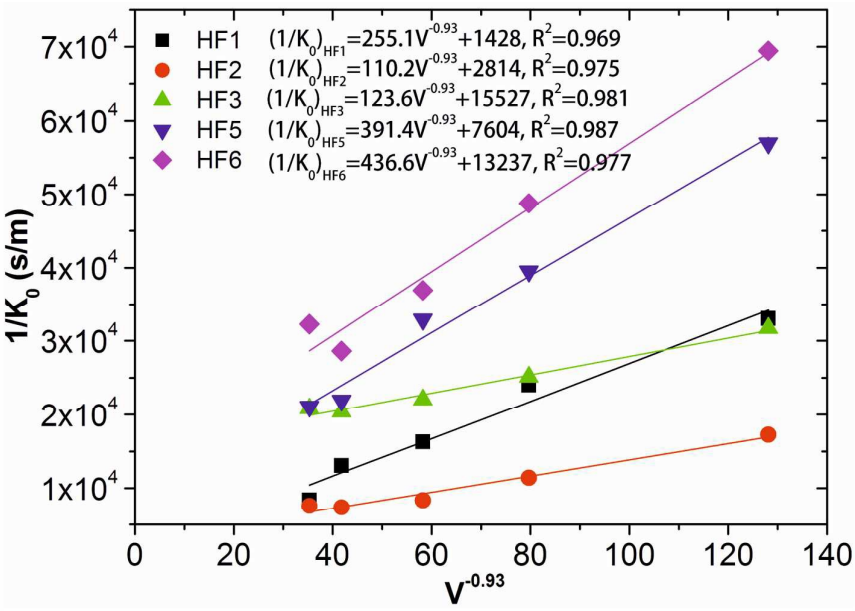

Figure 13. Wilson plot of the produced PVDF HFMs (pure CO_2-distilled water system).

Based on the graphs of Fig. 12, HFMs produced from PVDF1, *i.e.* HF1 and HF2, achieve significantly higher CO_2 absorption efficiency. This enhanced capability becomes more pronounced for HF1 and HF2 particularly at higher absorbent velocities. Comparing SEM images of HF1 and HF2 (Figs. 3-4) with those of HF4, HF5, HF6 (Figs. 7-9), the following structural parameters can explain the observed discrepancy:

- The great contribution of sub-layer large cavities to morphology of HF1-HF3 as schematically represented in Fig. 6.
- The morphology of independent cellular pores observed for HF4-HF6 (Figs. 7d-9d) versus morphology of interconnected pores within the HF1-HF3 structures (Figs. 3d-5d)

The above-mentioned structural parameters cause less resistance to be imposed by HFM structure against mass transfer. Therefore, enhanced CO_2 absorption is expected.

The difference in performances of HF1 and HF2 to capture CO_2 is also noticeable and can be assigned to the presence of macrovoids in the vicinity of outer surface layer of HF2 (see Fig. 4a) which are absent in Fig. 3a. Surprisingly, despite the presence of sub-layer cavity as well as macrovoids underneath the surface layer of HF3, this HF creates the largest membrane mass transfer resistance (Table 6) and unexpected N_2 permeance (Fig. 11) and CO_2 absorption (Fig. 12) comparable to HF5 and HF6. This as shown in Fig. 5d may be attributed to the relatively small interconnected pores enclosed in the polymer matrix.

As consequence, in Table 7, two PVDF HFs produced in the present work, HF2 and HF6, have been compared with PVDF HFs produced and investigated in literature focusing on their structural properties as well as CO_2 absorption performance. Data tabulated in Table 7 vividly point to significantly enhanced CO_2 absorption by the super-fine HFs produced in the present contribution. Comparison the performance of produced PVDF HFs with those of

commercially available PTFE and PP HFs provides further evidence for this claim as shown in Table 8. The fineness of produced HFs and presence of sub-layer cavities and macrovoids could primarily account for this remarkable improvement encountered in CO_2 capture.

Table 7. A comparison of structural properties and maximum CO_2 flux of the PVDF HFs (HF2 & HF6) produced in this work with those reported in the literature for PVDF HFs

Reference	*i.d./o.d.* (μm)	Overall porosity (%)	$\frac{\varepsilon}{L_P}$ (1/m)	r_P (nm)	Absorbent flow rate (ml/min)	CO_2 flux (mol/m^2.s)	HFM mass transfer resistance (s/m)	CEP_w (bar)	Collapsing pressure (bar)	Manufacturing/ Modification process
[4]	500/950	NA	623	126	300	7×10^{-4}	86315	4	NA	Surface modification using SMM
[6]	660/1080	NA	NA	NA	12.4	4.8×10^{-3} *	NA	NA	NA	TIPS
[7]	NA	77	1550 (10^2 m^{-1})	9.60	320	8×10^{-4}	12214	4.5	4	Using additive: Glycerol
[18]	514/828	76.02	NA	20	V_l=0.5 m/s	1.3×10^{-3} **	7930.9	NA	NA	Using additive: Phosphorous acid
[21]	550/1000	70.83	1070 (10^2 m^{-1})	2.33	200	1.6×10^{-3}	19637	5.33	NA	Using additive: $LiCl.H_2O$
[28]	415-493/780-837	76±1.8	467.4	13.6	300	1.4×10^{-3}	1503	5	7	Surface modification using SMM
Present work (HF2)	214/356	75.9	52.4	448	200	1.0×10^{-2}	2814	4	4	Additive-free solution
Present work (HF6)	235/407	75.4	17.5	896	200	2.39×10^{-3}	13237	5	5	Additive-free solution

* liquid absorbent: monoethanolamine (MEA), ** liquid absorbent: N_2 saturatd distilled water

Table 8. A comparison of structural properties and maximum CO_2 flux of the PVDF HFs (HF2 & HF6) produced in this work with those of commercially available PTFE and PP HFs

HF	*i.d./o.d.* (μm)	Absorbent flow rate (ml/min)	CO_2 flux (mol/m^2.s)	Manufacturer
Commercially available PTFE HFs [20]	1000/2000	200	3.0×10^{-4}	Sumitomo Electric Fine Polyme
Commercially available PP HFs [20]	240/300	200	1.25×10^{-4}	Mitsubishi Rayon
PVDF HFs (HF2)	214/356	200	1.0×10^{-2}	This work
PVDF HFs (HF6)	235/407	200	2.39×10^{-3}	This work

3.2. Rationalization of prepared HFs morphologies

As was stated previously, structurally different superfine PVDF HFs were prepared by alteration of PVDF and solvent type in conjunction with employing a high drawing ratio during HF fabrication. Discussed below is an attempt to rationalize the obtained morphologies relying on the phase behavior of ternary water/solvent/PVDF systems and viscoelastic properties of PVDF dopes and gels.

During membrane formation based on NIPS (nonsolvent-induced phase separation) technique, the initially homogeneous polymer solution is brought into contact with nonsolvent, commonly water. Through a period of time, solvent outflow and nonsolvent inflow make the polymer solution thermodynamically unstable. At this condition, the polymer solution separates into two coexisting liquid phases in thermodynamic equilibrium, *i.e.* polymer-rich and polymer-lean phases. The former eventually leads to the pores distributed in a matrix of the latter. This type of phase separation mechanism is known as liquid-liquid (L-L) phase separation. In the case of semi-crystalline polymers like PVDF, the polymer solution may also precipitate with respect to polymer crystallization where polymer crystals, solid phase (S), are in equilibrium with a liquid phase (L) whose composition locates on the crystallization-induced gelation boundary in ternary phase diagram. This mechanism is known as S-L phase separation [31, 48]. Prove has shown that using solutions of semi-crystalline polymers, the final morphology of membrane strongly depends on the outcome of competition between L-L and S-L phase separation mechanisms [31, 41, 49, 50]. Additionally, after occurrence of phase separation, the final morphology is strongly influenced by the further evolution of phase-separated domains. This event may be restricted depending on the viscoelastic characteristics of polymer-rich phases which has been explained in details in Refs. [38, 51].

Formation of macrovoids and large cavities is another controversial issue faced up during membrane synthesis and elaboration. As demonstrated in literature [52-54], liquid interfaces are subjected to convective flows associated with mass transfer within the vicinity of the interfacial region. Convective flows are driven by density gradient and/or gradient in interfacial energy. Considering membrane construction based on the phase inversion method, the convective flow of nonsolvent through the polymer solution driven by the interfacial energy gradient, is responsible for the formation of macrovoids and cavities [52, 55-57]. Overall, for convective flows to contribute the macrovoids as well as cavities formation and growth, the following prerequisite conditions must be met:

- Adequate supply of nonsolvent to polymer solution/nonsolvent interface to ensure the occurrence of convective flow
- Low resistance of surface layer against nonsolvent ingress and convective flows
- Relatively low viscosity of polymer solution

In light of the above facts, the main contributing events and factors to morphology evolution within PVDF HFs are as follow:

- L-L phase separation
- S-L phase separation, *i.e.* crystallization-induced gelation
- Rheological properties of PVDF dopes and gels

To clarify how above-mentioned factors are involved in the structure formation of PVDF HFs, construction of ternary phase diagram is the first step. Included in Fig. 14 are ternary phase diagrams of various water/DMF, NMP or 2P/PVDF1 ternary systems investigated in this work. The procedure to calculate these diagrams has been explained in section 2.2.

As seen in Fig. 14, for all systems the experimentally measured cloud points are reasonably in agreement with the theoretically calculated binodal boundaries through which the S-L miscibility gap is separated from L-L miscibility gap. Inside the S-L miscibility gap, the polymer solution becomes ultimately a gel; whereas a mixture within L-L immiscibility area experiences phase demixing into two liquid phases. As compared in Fig. 14d, when 2P is considered as solvent the binodal curve is positioned at distance farthest from the solvent/polymer axis. This corresponds to delayed L-L demixing. This distance becomes short and shorter when NMP and DMF are employed, respectively, which correspond to expedited L-L phase inversion. Differences in binodal locations stem predominantly from χ_{23} values compared in Table 1. As discussed in our previous studies [37, 40, 51, 58], smaller χ_{23} favors higher tendency of polymer to mix with solvent corresponding to higher amount of nonsolvent to bring about the L-L phase separation, *i.e.* delayed L-L demixing.

In contrast to binodal, as is shown in Fig. 14d, solvent type hardly changes the position of crystallization-induced gelation boundaries. This indicates that almost the same quantity of water is required for precipitation of PVDF1-based solution with respect to polymer crystallization. Therefore, it seems reasonable to postulate that the morphological variations observed among spun PVDF HFs are controlled by kinetics of L-L phase separation together with rheological properties of PVDF spinning solutions and dopes. Furthermore, regardless of solvent type, all of monitored structures depict a circumstance where L-L phase separation occurs in advance of PVDF crystallization. It is emphasized that similar phase diagrams (not shown) for corresponding solvents were also constructed for PVDF2-based systems. This highlights the inability of the ternary phase diagrams to entail the rheological properties of PVDF solutions. Strictly speaking, rheological images have to be superimposed on ternary phase diagrams to afford a powerful and comprehensive tool to predict the morphology of membranes prepared using phase inversion technique.

Further evidence indicating to accelerated L-L demixing for solutions composed of DMF was obtained by comparison of the normalized FTIR spectra of prepared HFs as illustrated in Fig. 15. The peaks centered at wavenumbers of 614, 765 and 975 cm^{-1} are assigned to α-phase with chain conformations of short trans sequence. Appeared bands at 840 and 1275 cm^{-1} are considered to monitor the evolution of β-phase in which polymer chains with conformations characterized by long trans sequences can be packed. γ-phase can be best followed using bands at 809 and 1233 cm^{-1} [43, 59, 60]. As evident, irrespective of PVDF type, PVDF1 or PVDF2, the intensities of α- and β-related peaks vary with solvent type in opposite directions as follows:

- Intensities of α-related peaks: DMF>NMP>2P
- Intensities of β-related peaks: DMF<NMP<2P

The ascending order of β-related peaks intensities for solvents used, fully corresponds with the increasing order of the distance between binodal and the solvent/polymer axis as DMF<NMP<2P (Fig. 14d). This concurrence further implies that L-L demixing takes place in faster and slower rates for DMF- and 2P-based solutions, respectively. The L-L demixing rate for NMP-based solution lies midway between those of DMF- and 2P-based solutions accordingly. In other words, formation of crystals happens when enough water is imbibed into the PVDF/solvent spinning solution and the crystallization-induced gelation boundary is crossed. However, the β crystals are enhanced when L-L demixing is delayed. This can be interpreted by the fact that after formation of polymer-rich domains as a direct consequence of L-L phase inversion, the mobility of polymer chains in the polymer-rich phases dramatically diminishes. Therefore, it becomes impossible for polymer chains to be further stretched and adopt conformations associated with longer trans sequences during the stretching process of spinning jet.

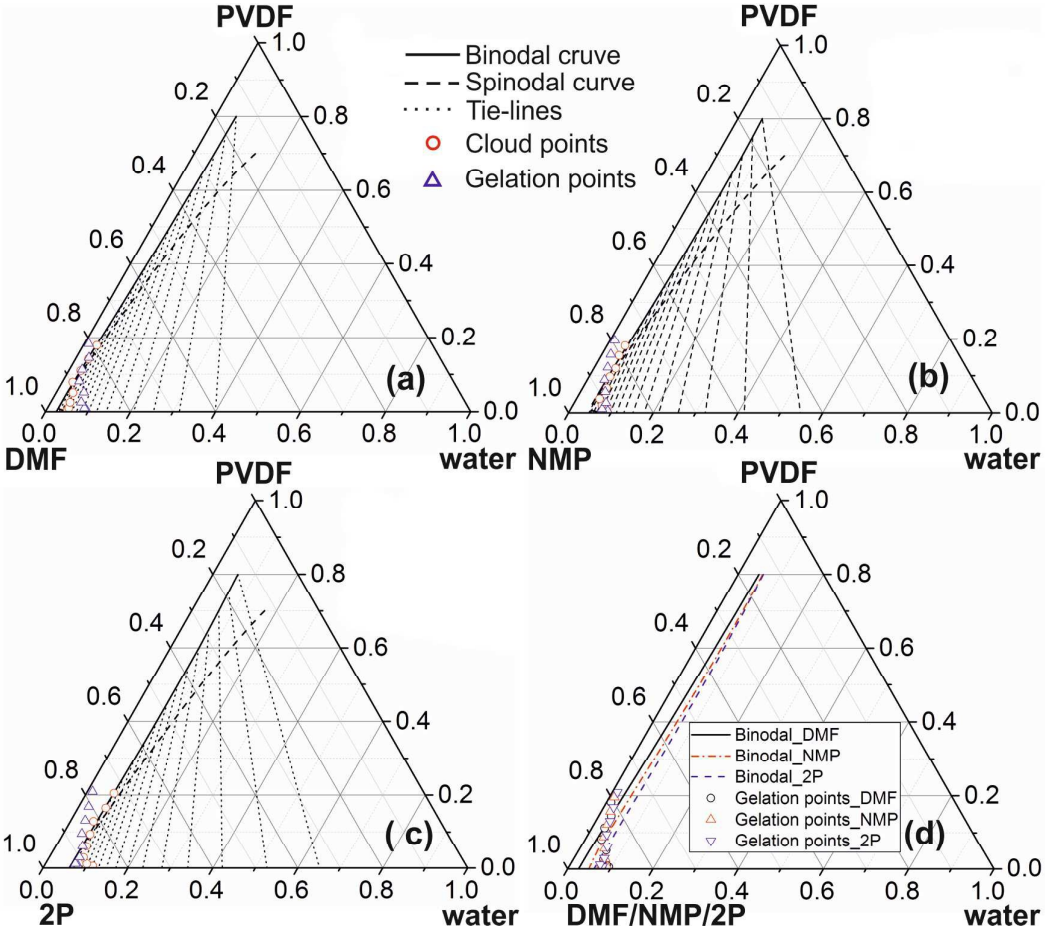

Figure 14. Ternary phase diagram of different ternary nonsolvent/solvent/polymer systems: (a) water/DMF/PVDF, (b) water/NMP/PVDF, (c) water/2P/PVDF, (d) Comparison locations of binodal and crystallization-induced gelation boundaries of various ternary systems.

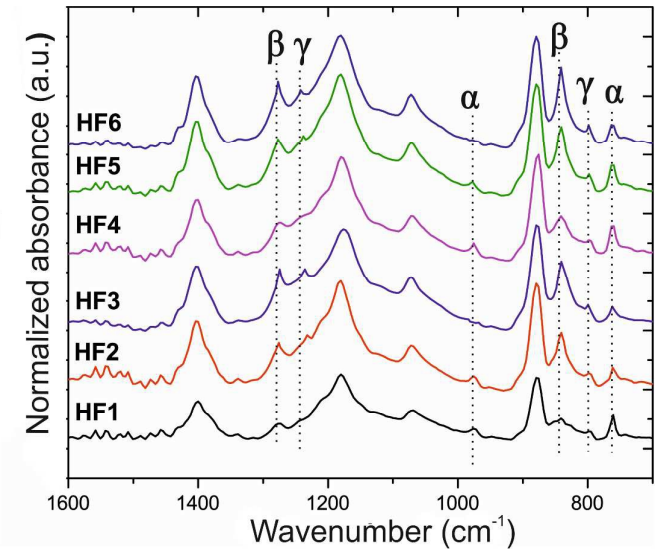

Figure 15. Normalized FTIR spectra of the prepared HFs.

The constructed ternary phase diagrams revealed the impressive ability of solvent to change the phase behavior of the investigated ternary systems. Although these diagrams would explain some observed structural differences, however, do not include the whole facts required to describe all the discrepancies in morphology of prepared HFs particularly those produced using the same solvent and different polymers (compare corresponding images in Figs. 3-5 and 8-10). Specifically, discussion about the corrugated inner contour of HFs and appearance of macrovoids as well as sub-layer cavities in skeleton of HF1-HF3 requires additional complementary rheological data. For this reason, the zero-shear viscosities of spinning solutions together with viscoelastic properties of some dopes as pointed in Fig. 16 were evaluated.

Table 2 lists the measured zero-shear viscosity (η_0) of the spinning solutions. It is confirmed, irrespective of PVDF type, the viscosities of spinning solutions follow an increasing order of $\eta_{0,PVDF/DMF} \ll \eta_{0,PVDF/NMP} < \eta_{0,PVDF/2P}$. Indeed, solutions made from PVDF1 show higher η_0 in comparison with those prepared from PVDF2. This is despite of the fact that PVDF1-based solutions have smaller φ_P, *i.e.* polymer volume fraction (refer to Table 2). This is the reason behind the shorter length of macrovoids beneath the outer surface of HF2 (Fig. 4a) and HF3 (Fig. 5a) in comparison to HF5 (Fig. 8a) and HF6 (Fig. 9a). These findings are similar to the results observed by Guillen *et al.* [55]. Considering HF1 (Fig. 3a) and HF4 (Fig. 7a) structures and despite of the relatively lower values of $\eta_{0,PVDF1/DMF}$ and $\eta_{0,PVDF2/DMF}$ (Table 2) it can be seen that macrovoids occupy very small areas in Figs. 3a-c & 8a-c. This is attributed to the accelerated L-L demixing of PVDF/DMF solutions during intimate contact with water as demonstrated by ternary phase diagram in Fig. 14a, d. This faster L-L phase inversion favors the formation of a surface layer with higher elastic modulus which is discussed later. Under these conditions, the initiated convective flows are dampened and therefore, macrovoids leave fewer imprints in the interior morphologies of HF1 and HF4.

As discussed earlier, HFs wet-spun from PVDF1 and PVDF2 solutions in the same solvent exhibited different morphologies despite the similarity of their ternary phase behavior. In order to provide a logical explanation to these discrepancies, the nascent HF structure was categorized into five layers, *i.e.* A_i or A_o, B_i, C_i, B_o and C_o as schematically illustrated in Fig. 19. This categorization is based on the concentration of coagulant imbibed by a specific layer. It is reasonable to assume that over a defined time span, the outer layers, *i.e.* C_i and C_o, experience the highest levels of solvent/nonsolvent exchange as a direct consequence of intimate contact with water both as bore fluid and external coagulant. The intensity of exchange reduces in the middle layers, *i.e.* A_i or A_o, B_i, B_o and C_o due to the imposed resistances by upper layers against diffusion of solvent and nonsolvent molecules. Hence, assuming the equal rates of solvent outflow and nonsolvent inflow throughout the HF structure, dopes A, B, C (Fig. 16) can roughly simulate the momentary situation of A_i, B_i, C_i or A_o, B_o, C_o layers (Fig. 19), respectively, during spinning.

The linear viscoelastic properties of dopes A, B, C including storage modulus (G'), loss modulus (G") and loss tangent (tan δ=G"/G') are depicted and compared in Figs. 17a1-a3. As can be seen, G' and G" are strongly frequency (ω)-dependent and exhibit an increasing trend with ω. In contrast, tan δ is a reducing function of ω. Such behavior implies that the response of dopes A, B, C to an imposed stress varies with the time scale of the deformation. Specifically, at higher frequencies corresponding to shorter time scale, dopes behave like elastic solids, whereas they act analogous to viscous fluids at lower frequencies. Similar behavior was also observed for water/Formic acid/Nylon6 system in our recently published paper [61]. These characteristics are unique features of viscoelastic liquids as fully explained in the literature [62-65]. Additionally, the relative magnitude of G' and G" is another issue to be considered. As argued in literature [62, 66], G">G' and tan δ>1 denote to prototypical liquid-like material while G'>G" and tan δ<1 along with less frequency-dependency of G'

feature prototypical solid-like material. Accordingly, it is a reasonable conjecture to postulate that moving from dope A to B and C despite the equal polymer concentration, *i.e.* $\varphi_{PVDF2} = 0.136$, with progress of both solvent outflow and nonsolvent inflow, the elastic modulus increases and eventually becomes less frequency-dependent. This corresponds to transition from liquid-like material to solid-like one (Fig. 17a1) for sequential order of A to B and C. Strictly speaking, during HF formation for a given time, outer layers (C_i and C_O) behave as solid-like materials with high G' which sequentially reduces inwards to the middle layers (A_i or A_o). Obviously, continuous exchange of solvent and nonsolvent as time elapses leads to increase in the G' of each layer.

On the basis of above information, it can be suggested that the formation of corrugated inner contour, sub-layer cavities and macrovoids can be elaborated by considering the interplay of convective flows and G' of outer layers (G'_o) in contact with bore fluid. The higher value of G'_o dampens the initiated convective flows and hence impedes the formation of corrugated inner contour, macrovoids and sub-layer cavities. In a detailed and exact way, it can be said the occurrence of convective flows is prevented when G'_o approaches a critical value, *i.e.* $G'_{o,critical}$ ($G'_o \geq G'_{o,critical}$). Therefore, the HF morphology is dominated by the priority of convective flow initiation and achieving$G'_{o,critical}$.

The above hypothesis can be verified by comparison of SEM images of HF4, HF5 and HF6 (Figs. 7a, 8a and 9a) produced from PVDF2-based solutions (points A, D, F in Fig. 16) as well as viscoelastic plots (Fig. 17b1-b3) of dopes B, E, G pointed in Fig. 16. In fact, since experimental determination of the composition of HF outer layer at a given time is very difficult, then for comparative purposes the following assumptions can assist further viscoelastic investigations:

- The outer layer is defined as the layer which is in intimate contact with bore fluid.

- Dopes B, E, G and M (pointed in Fig. 16) are considered as substitute compositions for outer layers of HF6, HF5, HF4 and HF1, respectively, at a given time elapsed after commencement of HF spinning, *e.g.* t_1.
- Dopes I, K, N (pointed in Fig. 16) are considered as substitute compositions for outer layers of HF3, HF2 and HF1, respectively, at a given time elapsed after commencement of HF spinning, *e.g.* t_2, $t_2 > t_1$.
- Longer given time since the commencement of HF spinning corresponds to higher concentration of nonsolvent imbibed by outer layers of HFs and hence longer distance of composition location in ternary phase diagram relative to solvent/polymer axis.

According to Figs. 17b1-b3, dopes B and E have similar values of G' and G" while those related to dope G are dramatically enhanced. Additionally, in contrast to dopes B and E, dope G behaves like solid material (tan δ<1) over the whole frequency range. This difference in viscoelastic properties of dopes B, E and G suitably explains the observed morphological differences between HF4, HF5 and HF6 as follows:

- In the case of HF5 and HF6, convective flows initiate before reaching to $G'_{o,critical}$ in outer layers, *i.e.* t_CF (time required to initiate convective flows)< $t\_G'_{o,critical}$ (time required to reach $G'_{o,critical}$ in outer layer of HF)
- In the case of HF4, achieving $G'_{o,critical}$ in outer layers of HF4 surpasses convective flows, *i.e.* $t\_CF > t\_G'_{o,critical}$.

Measured discrepancies between the viscoelastic behavior of dopes B, E and G with the same content of water can be best described by considering their locations on the ternary phase diagram (Fig. 16). Dopes B and E are positioned in the S-L miscibility gap of water/2P/PVDF2 and water/NMP/PVDF2 ternary phase diagrams, respectively. However, dope G locates after gelation and binodal boundaries of water/DMF/PVDF2 phase diagram.

This highlights the great contribution of phase behavior of ternary systems (compared in Fig. 14d) to time-resolved evolution of viscoelastic properties. Ternary phase behavior also reflects the differences between corresponding binary interaction parameters for two ternary systems composed of three components, nonsolvent (water), solvent (DMF, NMP or 2P) and polymer (PVDF1 or PVDF2). Hence, it seems reasonable to postulate that magnitude of G'_o and $G'_{o,critical}$ are not only severely influenced by PVDF and solvent types but also are dependent on binary interactions in ternary systems.

The viscoelastic properties of dopes I, K, N prepared using PVDF1 have been compared in Figs. 17c1-c3. Again the DMF-based dope, *i.e.* dope N, exhibits the highest values of G' and G". The second and third places belong to 2P- and NMP-based dopes. Compared with Figs. 17b1-b3 it can be stated that similar trend as that of dopes B, E and G, is also applicable to dopes I, k ,N. Contrarily, dopes I, K, N have greater G' and mimic solid-like materials (tan δ<1) irrespective of time scale of deformation. Nevertheless, surprisingly, HF3, HF2 and HF1 incorporate sub-layer large cavities in their structure (see Fig. 3a, 4a, 5a). This contrast was further investigated by comparing the viscoelastic properties of dope M (depicted in Fig. 16) with those of dopes N and G through Figs. 17d1-d3. It can be seen that G' of dope M is drastically lesser than that of dope G, despite their equal water content. This marked difference in magnitude of G' can be attributed to reduction in polymer concentration of dope M which facilitates the formation of sub-layer cavities within HF1. On the other hand, contrary to dope G, the G' of dope M is considerably lower than $G'_{o,critical}$ and dope M needs more water to exceed $G'_{o,critical}$ as observed for dope N. Under this condition, convective flow is permitted to act, thereby forming sub-layer large cavities. This is why sub-layer large cavities occupy the cross-section of HF1 (refer to Fig. 3a) while HF4 is empty of such structures (see Fig. 7a). Similar discussions can be followed to rationalize the appearance of sub-layer cavities as a main part of HF2 and HF3 structures (see Figs. 4a and 5a).

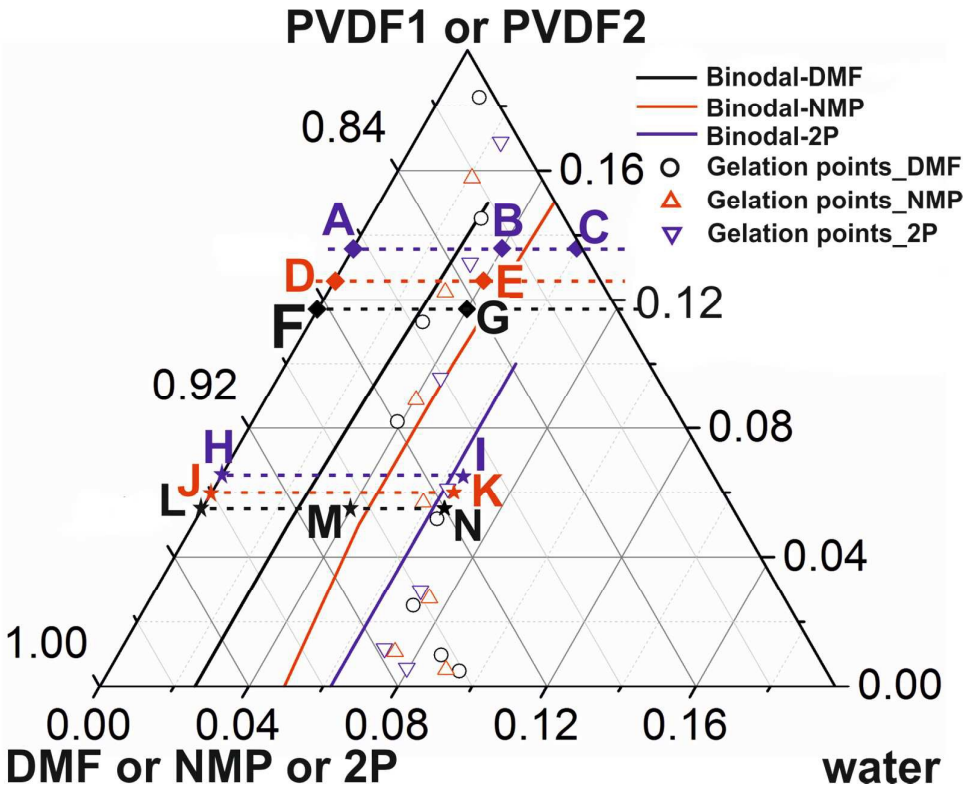

Figure 16. Localizing rheologically characterized dopes (A, B, C, E, G, I, K, M, N) as well as spinning dopes (A, D, F, H, J, L) on ternary phase diagram. Composition of dopes (A): $\varphi_{water} = 0, \varphi_{2P} = 0.864, \varphi_{PVDF2} = 0.136$, (B): $\varphi_{water} = 0.04, \varphi_{2P} = 0.842, \varphi_{PVDF2} = 0.136$, (C): $\varphi_{water} = 0.06, \varphi_{2P} = 0.804, \varphi_{PVDF2} = 0.136$, (D): $\varphi_{water} = 0, \varphi_{NMP} = 0.874, \varphi_{PVDF2} = 0.126$, (E): $\varphi_{water} = 0.04, \varphi_{NMP} = 0.834, \varphi_{PVDF2} = 0.126$, (F): $\varphi_{water} = 0, \varphi_{DMF} = 0.883, \varphi_{PVDF2} = 0.117$, (G): $\varphi_{water} = 0.04, \varphi_{DMF} = 0.888, \varphi_{PVDF2} = 0.117$, (H): $\varphi_{water} = 0, \varphi_{2P} = 0.935, \varphi_{PVDF1} = 0.065$, (I): $\varphi_{water} = 0.065, \varphi_{2P} = 0.87, \varphi_{PVDF1} = 0.065$, (J): $\varphi_{water} = 0, \varphi_{NMP} = 0.94, \varphi_{PVDF1} = 0.06$, (K): $\varphi_{water} = 0.065, \varphi_{NMP} = 0.875, \varphi_{PVDF1} = 0.06$, (L): $\varphi_{water} = 0, \varphi_{DMF} = 0.945, \varphi_{PVDF1} = 0.055$, (M): $\varphi_{water} = 0.04, \varphi_{DMF} = 0.905, \varphi_{PVDF1} = 0.055$, (N): $\varphi_{water} = 0.065, \varphi_{DMF} = 0.88, \varphi_{PVDF1} = 0.055$. φ: polymer volume fraction.

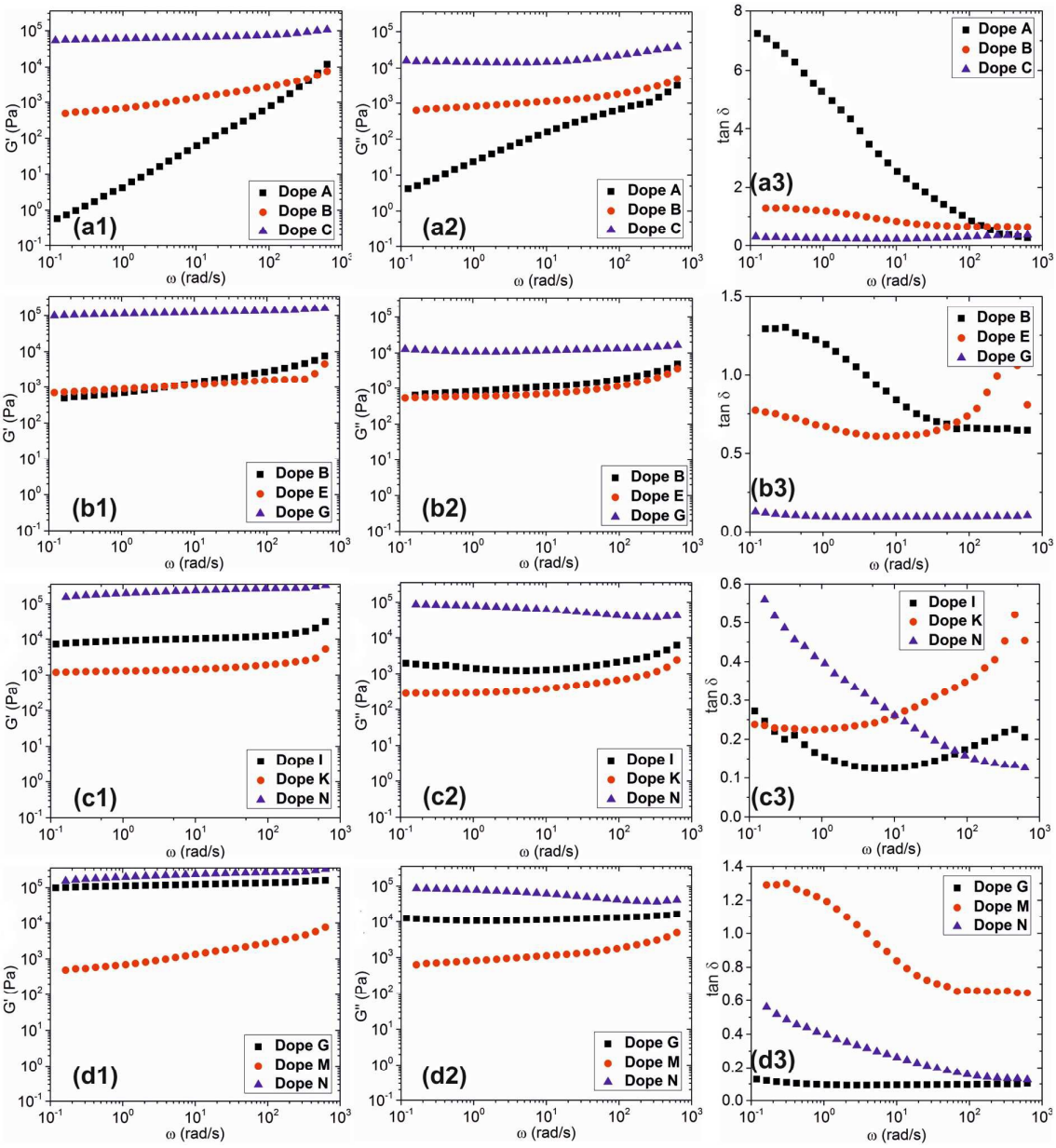

Figure 17. Viscoelastic properties, storage modulus (G'), loss modulus (G") and loss tangent (tan δ), of different dopes indicated by points A, B , C (a1-a3), B, E, G (b1-b3), I, K, M (c1-c3) and G, M, N (d1-d3) superimposed on ternary phase diagram displayed in Fig. 16.

As argued in preceding sections, the enhanced CO_2 absorption of produced HFs mainly arises from their fineness and presence of large cavities within their structures. It is generally accepted that drawing during fiber spinning is a powerful tool that controls fiber fineness. Thus in order to establish the crucial effect of the take-up speed on fineness as well as

morphology of prepared HF, solution A (refer to Table 2 and Fig. 16) was spun under three take-up speeds, i.e. free fall, 10 m/min and 20 m/min. The SEM images of the spun HFs are shown in Fig. 18. As evident, increasing the take-up speed is accompanied by formation of sub-layer cavities and corrugated inner contour. Overall, the role of drawing process may be summarized as:

- Enhancement and acceleration of convective flows occurrence at higher take-up speeds
- Joining of the leading edges of waves and hence formation of enclosed cavities.

The above factors become intensified as G_o' is reduced and therefore larger cavities are expected. The formation of large cavities in HFs is schematically illustrated in Fig. 19.

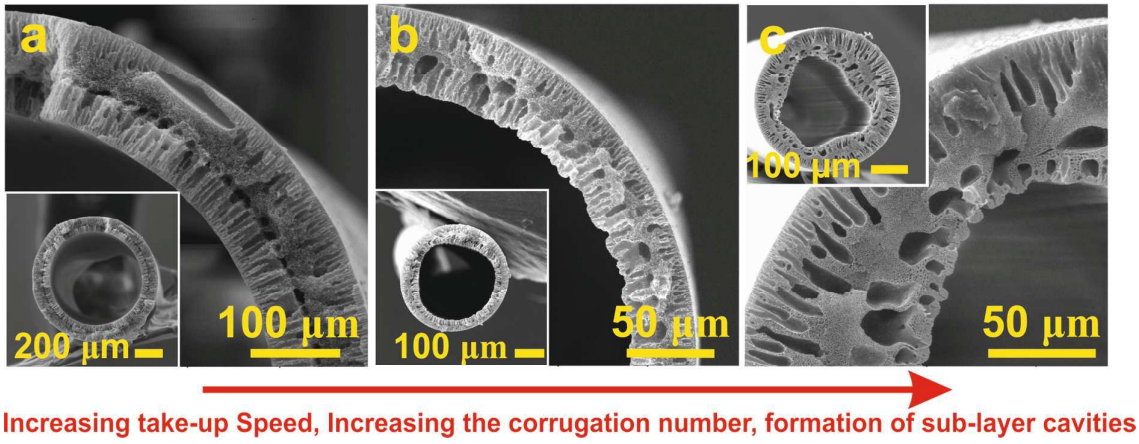

Figure 18. The effect of take-up speed on formation of cavities within PVDF HF structure: (a) free fall, (b) 10 m/min and (c) 20 m/min.

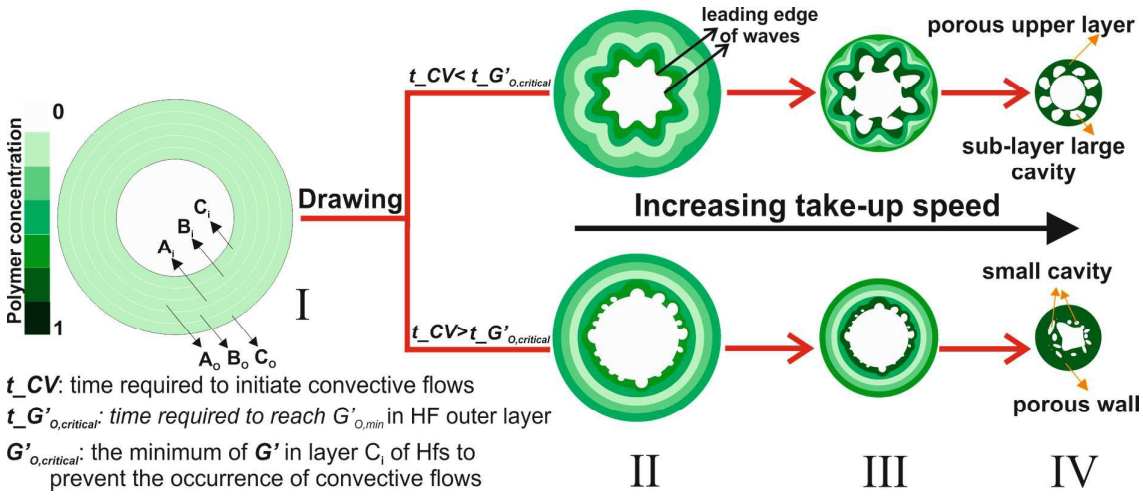

Figure 19. Schematic representation of large cavities formation within super-fine PVDF HF structure.

4. Conclusion

Super-fine PVDF HFs with astonishing CO_2 absorption capabilities were prepared using additive-free solutions with different ternary phase behavior and rheological properties. The results showed that the CO_2 absorption efficiency is directly related to the liquid absorbent flow rate. Furthermore, this relationship is strongly influenced by HF structure. Sub-layer large cavities and macrovoids impart superior CO_2 capture to the produced HFs particularly at higher absorbent flow rates. It was found that the following parameters contribute to enhancement of HF CO_2 capture:

- Presence of macrovoids in the vicinity of liquid-gas interfacial area
- Presence of sub-layer large cavity
- Replacement of independent cellular pores by interconnected network of pores in HF structure
- Absence of inner skin in the HF structure

Totally, it must be said that superfine HFs with structures composed of macrovoids and large cavities are more promising candidates for CO_2 absorption. This is due to replacing of polymer molecules with air in the macrovoids and cavities. Strictly speaking, the fineness as well as presence of the empty spaces, *i.e.* macrovoids and large cavities, reduces resistance against transfer of CO_2 molecules through thickness of HF wall and hence, more CO_2 is absorbed by liquid absorbent.

Superimposing rheological images on nonsolvent/solvent/PVDF ternary phase diagrams was firstly introduced and employed as a promising approach to rationalize resultant morphologies within manufactured HFs. It was demonstrated that the evolution and length of macrovoids is predominantly controlled by zero-shear viscosity of spinning solution. As well, evidence was obtained indicating that the formation of sub-layer large cavities in PVDF HFMs is promoted when the following requirements are met:

- The convective flows are allowed to act. This depicts the circumstance where the elastic modulus of outer layer of HF (G'_o) in intimate contact with bore fluid is lower than $G'_{o,critical}$ above which the convective flows are dampened. The parameters G'_o and $G'_{o,critical}$ are controlled by PVDF and solvent type along with three binary interactions between nonsolvent, solvent and polymer components.
- Producing HFs under the higher values of take-up speed through which the convective flows are probably enhanced and accelerated.

5. References

[1] P. Luis, T. Van Gerven, B. Van der Bruggen, Recent developments in membrane-based technologies for CO_2 capture, Prog. Energy. Combus. Sci. 38 (2012) 419-448.

[2] H. Herzog, B. Eliasson, O. Kaarstaed, Capturing greenhouse gases, Sci. Am. 282 (2000) 72-79.

[3] P. Riemer, Greenhouse gas mitigation technologies, an overview of the CO_2 capture, storage and future activities of the IEA greenhouse gas R&D programme, Energ. Convers. Manage. 37 (1996) 665-670.

[4] A. Mansourizadeh, Z. Aslmahdavi, A.F. Ismail, T. Matsuura, Blend polyvinylidene fluoride/surface modifying macromolecule hollow fiber membrane contactors for CO_2 absorption, Int. J. Greenh. Gas Con. 26 (2014) 83-92.

[5] A. Gabelman, S.T. Hwang, Hollow fiber membrane contactors, J. Membr. Sci. 159 (1999) 61-106.

[6] S. Rajabzadeh, Sh. Yoshimoto, M. Teramoto, M. Al-Marzoughi, H. Matsuyama, CO_2 absorption by using PVDF hollow fiber membrane contactors with various membrane structures, Sep. Purif. Technol. 69 (2009) 210-220.

[7] A.F. Ismail, A. Mansourizadeh, A comparative study on the structure and performance of porous polyvinylidene fluoride and polysulfone hollow fiber membranes for CO_2 absorption, J. Membr. Sci. 365 (2010) 319-328.

[8] N. Ghasem, M. Al-Marzoughi, A. Duidar, Effect of PVDF concentration on the morphology and performance of hollow fiber membrane employed as gas-liquid membrane contactor for CO2 absorption, Sep. Purif. Technol. 98 (2012)174-185.

[9] N. Nishikawa, M. Ishibashi, H. Ohta, N. Akutsu, H. Matsumoto, T. Kamata, H. Kitamura, CO_2 removal by hollow fiber gas-liquid contactor, Energ. Convers. Manage. 36 (1995) 415-418.

[10] S. Khaisri, D. deMontigny, P. Tontiwachwuthikul, R. Jiraratananon, Comparing membrane resistance and absorption performance of three different membranes in a gas absorption membrane contactor, Sep. Purif. Technol. 65 (2009) 290–297.

[11] R. Wang, H.Y. Zhang, P.H.M. Feron, D.T. Liang, Influence of membrane wetting on CO2 capture in microporous hollow fiber membrane contactors, Sep. Purif. Technol. 46 (2005) 33-40.

[12] N. Ghasem, M. Al-Marzouqi, L. Zhu, Preparation and properties of polyethersulfone hollow fiber membranes with o-Xylene as an additive used in membrane contactors for CO2 absorption, Sep. Purif. Technol. 92 (2012)1–10.

[13] M. Rahbari-Sisakht, A.F. Ismail, T. Matsuura, Development of asymmetric polysulfone hollow fiber membrane contactor for CO_2 absorption, Sep. Purif. Technol. 86 (2012) 215–220.

[14] M. Rahbari-sisakht, A.F. Ismail, T. Matsuura, Effect of bore fluid composition on structure and performance of asymmetric polysulfone hollow fiber membrane contactor for CO2 absorption, Sep. Purif. Technol. 88 (2012) 99–106.

[15] M. Rahbari-Sisakht, A.F. Ismail, D. Rana, T. Matsuura, Effect of different additives on the physical and chemical CO_2 absorption in polyetherimide hollow fiber membrane contactor system, Sep. Purif. Technol. 98 (2012) 472–480.

[16] R. Naim, A.F. Ismail, N.B. Cheer, M.S. Abdullah, Polyvinylidene fluoride and polyetherimide hollow fiber membranes for CO_2 stripping in membrane contactor, Chem. Eng. Res. Des. 92 (2014) 1391-1398.

[17] H.J. Lee, E. Magnone, J.H. Park, Preparation, characterization and laboratory-scale application of modified hydrophobic aluminum oxide hollow fiber membrane for CO_2 capture using H_2O as low-cost absorbent, J. Membr. Sci. 494 (2015) 143-153.

[18] S. Atchariyawut, C. Feng, R. Wang, R. Jiraratananon, D.T. Liang, Effect of membrane structure on mass-transfer in the membrane gas–liquid contacting process using microporous PVDF hollow fibers, J. Membr. Sci. 285 (2006) 272–281.

[19] J. Ren, R. Wang, H.Y. Zhang, Z. Li, D.T. Liang, J.H. Tay, Effect of PVDF dope rheology on the structure of hollow fiber membranes used for CO_2 capture, J. Membr. Sci. 281 (2006) 334–344.

[20] A. Xu, A. Yang, S. Young, D. deMontigny, P. Tontiwachwuthikul, Effect of internal coagulant on effectiveness of polyvinylidene fluoride membrane for carbon dioxide separation and absorption, J. Membr. Sci. 311 (2008) 153-158.

[21] A. Mansourizadeh, A.F. Ismail, T. Matsuura, Effect of operating conditions on the physical and chemical CO_2 absorption through the PVDF hollow fiber membrane contactor, J. Membr. Sci. 353 (2010) 192–200.

[22] A. Mansourizadeh, A.F. Ismail, Effect of LiCl concentration in the polymer dope on the structure and performance of hydrophobic PVDF hollow fiber membranes for CO_2 absorption, Chem. Eng. J. 165 (2010) 980–988.

[23] S. Wongchitphimon, R. Wang, R. Jiraratananon, Surface modification of polyvinylidene fluoride-co-hexafluoropropylene (PVDF–HFP) hollow fiber membrane for membrane gas absorption, J. Membr. Sci. 381 (2011)183– 191.

[24] A. Mansourizadeh, A.F. Ismail, Preparation and characterization of porous PVDF hollow fiber membranes for CO_2 absorption: Effect of different non-solvent additives in the polymer dope, Int. J. Greenh. Gas Con. 5 (2011) 640–648.

[25] M. Rahbari-Sisakht, A.F. Ismail, D. Rana, T. Matsuura, A novel surface modified polyvinylidene fluoride hollow fiber membrane contactor for CO_2 absorption, J. Membr. Sci. 415 (2012) 221–228.

[26] N. Ghasem, M. Al-Marzouqi, N. Abdul Rahim, Effect of polymer extrusion temperature on poly(vinylidene fluoride) hollow fiber membranes: Properties and performance used as gas–liquid membrane contactor for CO2 absorption, Sep. Purif. Technol. 99 (2012) 91–103.

[27] M. Rahbari-Sisakht, A.F. Ismail, D. Rana, T. Matsuura, D. Emadzadeh, Effect of SMM concentration on morphology and performance of surface modified PVDF hollow fiber membrane contactor for CO_2 absorption, Sep. Purif. Technol. 116 (2013) 67–72.

[28] F. Korminouri, M. Rahbari-Sisakht, D. Rana, T. Matsuura, A.F. Ismail, Study on the effect of air–gap length on properties and performance of surface modified PVDF hollow fiber membrane contactor for carbon dioxide absorption, Sep. Purif. Technol. 132 (2014) 601–609.

[29] M. Rezaei, A.F.Ismail, S.A.Hashemifard, T.Matsuura, Preparation and characterization of PVDF-montmorillonite mixed matrix hollow fiber membrane for gas–liquid contacting process, Chem. Eng. Res. Des. 92, 2449–2460, 2014.

[30] M. Rezaei, A.F. Ismail, S.A. Hashemifard, Gh. Bakeri, T. Matsuura, Experimental study on the performance and long-term stability of PVDF/montmorillonite hollow fiber mixed matrix membranes for CO_2 separation process, Int. J. Greenh. Gas Con. 26 (2014) 147–157.

[31] H. Fashandi, A. Yegane, M.M. Abolhasani, Interplay of liquid-liquid and solid-liquid phase separation mechanisms in porosity and polymorphism evolution within poly(vinylidene fluoride) nanofibers, Fiber. Polym. 16 (2015) 326-344.

[32] F. Liu, N.A. Hashim, Y. Liu, M.R. Moghareh Abed, and K. Li, Progress in the production and modification of PVDF membranes, J. Membr. Sci. 375 (2011) 1-27.

[33] H. Tompa, Polymer Solution. Butterworth Scientific. London. 1956.

[34] L. Yilmaz, A.J. McHugh, Analysis of nonsolvent-solvent-polymer phase diagrams and their relevance to membrane formation modeling, J. Appl. Polym. Sci. 31 (1986) 997-1018.

[35] F.W. Altena, C.A. Smolders, Calculations of liquid-liquid phase separation in a ternary system of a polymer in a mixture of solvent and a nonsolvent. Macromolecules, 15 (1982) 1491-1497.

[36] L. Zeman, G. Tkacik, Thermodynamic analysis of a membrane forming system water/N-methyl-2-pyrolidone/polyethersulfone, J. Membr. Sci. 36 (1988) 119-140.

[37] H. Fashandi, M. Karimi, Comparative studies on the solvent quality and atmosphere humidity for electrospinning of nanoporous polyetherimide fibers, Ind. Eng. Chem. Res. 53 (2014) 235−245.

[38] J.T. Tsai, Y.S. Su, D.M. Wang, J.L. Kuo, J.Y. Lai, A. Deratani, Retainment of pore connectivity in membranes prepared with vapor-induced phase separation, J. Membr. Sci. 362 (2010) 360–373.

[39] A. Bottino, G. Camera-Roda, G. Capannelli, S. Munari. The formation of microporous polyvinylidene fluoride membranes by phase separation, J. Membr. Sci. 57 (1991) 1-20.

[40] H. Fashandi, M. Karimi, Pore formation in polystyrene fiber by superimposing temperature and relative humidity of electrospinning atmosphere, Polymer. 53 (2012) 5832-5849.

[41] L.P. Cheng, D.J. Lin, C.H. Shin, A.H. Dwan, C.C. Gryte, PVDF membrane formation by diffusion-induced phase separation-morphology prediction based on phase behavior and Mass Transfer Modeling, J. Polym. Sci. B: Polym. Phys. 37 (1999) 2079–2092.

[42] K. Li, Ceramic membranes for separation and reaction, John Wiley and Sons, 2007.

[43] L. Yu, P. Cebe, Crystal polymorphism in electrospun composite nanofibers of poly (vinylidene fluoride) with nanoclay, Polymer. 50 (2009) 2133-2141.

[44] E.E. Wilson, A basis for rational design of heat transfer apparatus, Trans. ASME. 37 (1915) 47-82.

[45] V.Y. Dindore, D.W.F. Brilman, P.H.M. Feron, G.F. Versteeg, CO_2 absorption at elevated pressures using a hollow fiber membrane contactor, J. Membr. Sci. 235 (2004) 99–109.

[46] H.C. Shin, H.C. Shin, Y.S. Yeh, H. Yasuda, morphology of microporous poly(vinylidene fluoride) membranes studied by gas permeation and scanning microscopy, J. Membr. Sci. 50 (1990) 299-317.

[47] M.C. Yang, E.L. Cussler, Designing hollow-fiber contactors, AIChE J. 32 (1986) 1910-1916.

[48] T.H. Young, D.J. Lin, J.J. Gau, W.Y. Chuang, L.P. Cheng, Morphology of crystalline Nylon-610 membranes prepared by the immersion-precipitation process: competition between crystallization and liquid–liquid phase separation, Polymer. 40 (1999) 5011-5021.

[49] X. Li, Y. Wang, X. Lu, C. Xiao, Morphology changes of polyvinylidene fluoride membrane under different phase separation mechanisms, J. Membr. Sci. 320 (2008) 477-482.

[50] L.P. Cheng, Effect of temperature on the formation of microporous PVDF membranes by precipitation from 1-octanol/DMF/PVDF and water/DMF/PVDF systems. Macromolecules. 32 (1999) 6668-6674.

[51] H. Fashandi, A.R. Ghomi, Interplay of Phase Separation and Physical Gelation in Morphology Evolution within Nanoporous Fibers Electrospun at High Humidity Atmosphere, Ind. Eng. Chem. Res. 54 (2014) 240-253.

[52] M.A. Frommer, R.M. Messalem, Mechanism of membrane formation. 6. convective flows and large void formation during membrane precipitation, Ind. Eng. Chem. Prod. Res. Dev. 12 (1973) 328-333.

[53] T.K. Sherwood, J.C. Wei, Interfacial phenomena in liquid extraction, Ind. Eng. Chem. 49 (1957) 1030-1034.

[54] J.R.A. Pearson, On convection cells induced by surface tension, J. Fluid Mech. 4 (1958) 489-500.

[55] G.R. Guillen, G.Z. Ramon, H.P. Kavehpour, R.B. Kaner, E.M.V. Hoek, Direct microscopic observation of membrane formation by nonsolvent induced phase separation, J. Membr. Sci. 431 (2013) 212-220.

[56] R. Matz, The structure of cellulose-acetate membrane. 1. Development of porous structures in anisotropic membranes. Desalination. 10 (1972) 1-15.

[57] S. Bonyadi, T.S. Chung, W.B. Krantz, Investigation of corrugation phenomenon in inner contour of hollow fibers during the non-solvent induced phase-separation process, J. Membr. Sci. 299 (2007) 200-210.

[58] H. Fashandi, M. Karimi, Evidence for the impression of phase behavior of nonsolvent/solvent/polymer ternary system on morphology of polyethersulfone electrospun nanofibers, Fiber. Polym. 15 (2014) 1375-1386.

[59] P. Martins, A.C. Lopes, S. Lanceros-Mendez, Electroactive phases of poly (vinylidene fluoride): Determination, processing and applications, Prog. Polym. Sci. 39 (2014) 683-706.

[60] W.A. Yee, M. Kotaki, Y. Liu, X. Lu, Morphology, polymorphism behavior and molecular orientation of electrospun poly (vinylidene fluoride) fibers, Polymer. 48 (2007) 512-521.

[61] H. Fashandi, K. Zarrini, M. Youssefi, M.M. Abolhasani, Synergistic contribution of spinneret diameter and physical gelation to develop macrovoid-free hollow fiber membranes using single orifice spinneret. Ind. Eng. Chem. Res. 54 (2015) 7728–7736.

[62] R.G. Larson, The structure and rheology of complex fluids, Oxford University Press, New York, 1999.

[63] L. Li, Y. Aoki, Rheological images of poly(vinyl chloride) gels. 1. the dependence of sol-gel transition on concentration, Macromolecules. 30 (1997) 7835-7841.

[64] W. Du, H. Chen, H. Xu, D. Pan, N. Pan, Viscoelastic behavior of polyacrylonitrile/dimethylsulfoxide concentrated solution with water, J. Polym. Sci. B: Polym. Phys. 47 (2009) 1437-1442.

[65] L. Tan, H. Chen, D. Pan, N. Pan, Investigation into the gelation and crystallization of polyacrylonitrile. Eur. Polym. J. 45 (2009) 1617-1624.

[66] L. Shen, Y. Lin, Q. Du, W. Zhong, Y. Yang, Preparation and rheology of polyamide-6/attapulgite nanocomposites and studies on their percolated structure. Polymer. 46 (2005) 5758-5766.